Title: An immunohistochemical atlas of necroptotic pathway expression

Authors: Shene Chiou[1,2,^], Aysha H. Al-Ani[1,2,3,^], Yi Pan[1], Komal M. Patel[1], Isabella Y. Kong[4], Lachlan W. Whitehead[1,2], Amanda Light[1], Samuel N. Young[1], Marilou Barrios[1,2], Callum Sargeant[1,2], Pradeep Rajasekhar[1,2], Leah Zhu[1], Anne Hempel[1], Ann Lin[1], James A. Rickard[1,6], Cathrine Hall[1], Pradnya Gangatirkar[1], Raymond K.H. Yip[1,2], Wayne Cawthorne[1,2], Annette V. Jacobsen[1,2], Christopher R. Horne[1,2], Katherine R. Martin[7], Lisa J. Ioannidis[1,2], Diana S. Hansen[1,2,5], Jessica Day[1,2,3], Ian P. Wicks[1,2], Charity Law[1,2], Matthew E. Ritchie[1,2], Rory Bowden[1,2], Joanne M. Hildebrand[1,2], Lorraine A. O'Reilly[1,2], John Silke[1,2], Lisa Giulino-Roth[4], Ellen Tsui[1], Kelly L. Rogers[1,2], Edwin D. Hawkins[1,2], Britt Christensen[1,2,3], James M. Murphy[1,2,7,*] and André L. Samson[1,2,*].

Affiliations: [1]Walter and Eliza Hall Institute of Medical Research, Parkville, Australia

[2]University of Melbourne, Parkville, Australia

[3]Royal Melbourne Hospital, Parkville, Australia

[4]Pediatric Hematology/Oncology, Weill Cornell Medical College, New York, USA

[5]Monash Biomedicine Discovery Institute, Department of Microbiology, Monash University, Clayton, Australia

[6]Austin Hospital, Heidelberg, Australia

[7]Drug Discovery Biology, Monash Institute of Pharmaceutical Sciences, Parkville, Australia

[^]These authors contributed equally to this work

*Joint senior and corresponding authors: jamesm@wehi.edu.au (JMM) and samson.a@wehi.edu.au (ALS).

Highlights:

- 13 automated immunohistochemistry protocols for detecting the necroptotic pathway
- Necroptotic pathway expression is confined to fast-cycling immune barriers
- Necroptotic pathway expression changes at sites of immunoinflammatory challenge
- Immunodetection of necrosomes in IBD patients is a putative new diagnostic tool

Abstract: Necroptosis is a lytic form of regulated cell death reported to contribute to inflammatory diseases of the gut, skin and lung, as well as ischemic-reperfusion injuries of the kidney, heart and brain. However, precise identification of the cells and tissues that undergo necroptotic cell death *in vivo* has proven challenging in the absence of robust protocols for immunohistochemical detection. Here, we provide automated immunohistochemistry protocols to detect core necroptosis regulators – Caspase-8, RIPK1, RIPK3 and MLKL – in formalin-fixed mouse and human tissues. We observed surprising heterogeneity in protein expression within tissues, whereby short-lived immune barrier cells were replete with necroptotic effectors, whereas long-lived cells lacked RIPK3 or MLKL expression. Local changes in the expression of necroptotic effectors occurred in response to insults such as inflammation, dysbiosis or immune challenge, consistent with necroptosis being dysregulated in disease contexts. These methods will facilitate the precise localisation and evaluation of necroptotic signaling *in vivo*.

Main text:

Introduction

The necroptotic cell death pathway leads to cell lysis and expulsion of cellular contents into the extracellular milieu, which in turn provokes an innate immune response. Necroptosis is considered to be an altruistic cell death pathway whose principal role is to protect the host from pathogens (Fletcher-Etherington *et al*, 2020; Liu *et al*, 2021; Palmer *et al*, 2021; Pearson *et al*, 2017; Petrie *et al*, 2019; Upton *et al*, 2010; Yeap & Chen, 2022; Zhang *et al*, 2020). Despite this, it is the aberrant functions of necroptosis associated with inflammatory diseases that have spurred interest in its underlying mechanisms and therapeutic prospects (Choi *et al*, 2019; Fang *et al*, 2021). Studies of mice lacking the terminal effectors of the pathway – RIPK3 (Receptor-interacting protein kinase-3) or MLKL (Mixed-lineage kinase domain-like) – have led to the concept that excess necroptosis drives a range of inflammatory pathologies in organs including the skin, gut, brain, heart, lung, kidney and testes (Devos *et al*, 2020; Gunther *et al*, 2011; Ito *et al*, 2016; Li *et al*, 2017; Linkermann *et al*, 2013; Lu *et al*, 2021; Luedde *et al*, 2014; Naito *et al*, 2020). However, many of these attributions have been disputed (Dominguez *et al*, 2021; Newton *et al*, 2016; Wang *et al*, 2020b), likely reflecting an evolving understanding of the pathway and the limited availability of validated reagents to interrogate necroptosis in pathological specimens.

The core signaling axis of the necroptotic pathway has been well-defined and can be activated in response to a variety of inflammatory cues including ligation of Death, Toll-like or Pathogen-Pattern receptors (Chen *et al*, 2022b; Cho *et al*, 2009; Degterev *et al*, 2008; He *et al*, 2011; He *et al*, 2009; Kaiser *et al*, 2013; Kaiser *et al*, 2011). Caspase-8 is a critical negative regulator of necroptotic signaling (Kaiser *et al.*, 2011), whereby its deletion or loss-of-function promotes oligomerisation of RIPK1 (Receptor-interactor protein kinase-1), TRIF (TIR domain-containing adapter molecule 1) and/or ZBP1 (Z-DNA-binding protein

1) (Kaiser *et al.*, 2013). This oligomeric structure, otherwise known as the necrosome, promotes activation of the downstream effectors RIPK3 and MLKL (Samson *et al*, 2021b). RIPK3 recruits the MLKL pseudokinase to the necrosome, where it phosphorylates MLKL to provoke a conformational change, release from the necrosome, oligomerization and trafficking to the plasma membrane (Garnish *et al*, 2021; Murphy *et al*, 2013; Samson *et al*, 2020; Sun *et al*, 2012; Wang *et al*, 2014; Zhao *et al*, 2012). At the plasma membrane, accumulation of activated MLKL to a critical threshold level is required for membrane permeabilization via a poorly understood mechanism that brings about the cell's demise (Chen *et al*, 2014; Hildebrand *et al*, 2014; Samson *et al.*, 2020).

As our understanding of the necroptosis pathway has grown, new tools and protocols have been developed to study necroptotic signaling in fixed cultured cells (Rodriguez *et al*, 2016; Samson *et al*, 2021a; Wang *et al.*, 2014; Webster *et al*, 2018). However, robust procedures for assessing the necroptotic pathway in tissues are still lacking, often leading to contradictory reports in the literature and misattributions of necroptotic pathologies. Here, we report automated immunostaining protocols for detecting Caspase-8, RIPK1, RIPK3 and MLKL, in mouse formalin-fixed paraffin-embedded tissues. These procedures have enabled the assembly of an atlas of necroptotic pathway expression in mouse tissues under basal conditions and during innate immune challenge. While the necroptosis machinery is rarely expressed in cell types other than short-lived barrier cells, sterile inflammation increased RIPK3 expression in the gut and liver, broadly predisposing multiple cell types to necroptotic death. In contrast, elimination of the intestinal microflora diminished ~~RIPK3~~ expression of RIPK3 and MLKL to reduce necroptotic propensity in the gut. RIPK3 is also uniquely upregulated in splenic germinal centres suggesting it may have a non-necroptotic role in humoral immunity. Furthermore, we present robust protocols for detecting human Caspase-8, RIPK1, RIPK3 and MLKL and illustrate their utility for detecting dysregulated necroptosis in biopsies from patients

with inflammatory bowel disease (IBD). Collectively, these protocols will empower the definitive evaluation of where and when necroptosis occurs in vivo in health and disease.

Results:

Standardised immunohistochemical detection of the necroptotic pathway in mouse tissues

We recently compiled a toolbox of immunofluorescence assays to detect necroptotic signaling in cells (Samson *et al.*, 2021a). This toolbox requires use of: 1) non-crosslinking fixatives and 2) gene knockouts to account for non-specific signals; requirements that often cannot be met when immunostaining tissues. Here we aimed to develop robust immunohistochemistry protocols to detect the necroptotic pathway in formalin-fixed paraffin-embedded mouse tissues. Embedding and immunostaining was performed in an automated manner (see *Methods*) to allow reliable and scalable detection of the necroptotic pathway, and to lessen the future need to account for non-specific immunosignals using appropriate gene knockout controls. The specificity of thirteen monoclonal antibodies against Caspase-8, RIPK1, RIPK3 or MLKL was first tested by immunoblotting spleen homogenates from wild-type versus knockout mice (Fig. **EV1**). The intensity and specificity of antibodies for immunohistochemistry was then iteratively optimised across 21 conditions (see *Methods* and Fig. **EV1**). At each optimisation step, immunohistochemical signals from the spleen of wild-type versus knockout mice were quantified (Fig. **1Ai**), ratioed (Fig. **1Aii**) and integrated to yield an index of performance (Fig. **1Aiii**). For example, this pipeline improved the detection of RIPK1 with the monoclonal antibody D94C12 by approximately three orders of magnitude (Fig. **EV1**). In total, seven automated immunohistochemistry protocols to detect mouse Caspase-8, RIPK1, RIPK3 or MLKL were developed (Fig. **1B**). The detection of Caspase-8, RIPK1 and RIPK3 using these immunohistochemistry protocols (Fig. **1B**) closely aligned with the abundance of these proteins across multiple tissues as measured by high-resolution quantitative mass spectrometry (Fig. **1C**), indicating both specificity and sensitivity. Despite many rounds of optimisation with three specific anti-MLKL antibodies, mouse MLKL

remained difficult to detect via immunohistochemistry in all tissues except the spleen (Fig. **1B,D** and **EV1**).

Basal expression of the necroptotic pathway is restricted to fast-cycling immune barriers.

The immunohistochemical profile of Caspase-8, RIPK1, RIPK3 and MLKL across seven different organs suggested that expression of the necroptotic pathway is heavily restricted in unchallenged mice (Fig. **1D**). For example, RIPK3^{+} cells were scarce in the kidney and heart, and RIPK3 was undetectable in the brain (Fig. **1D**). By comparison, co-expression of Caspase-8, RIPK1 and RIPK3 was evident in intestinal epithelial cells, some splenic regions and Kupffer cells (Fig. **2A**). The *Tabula Muris* single cell RNA sequencing dataset supports the conclusion that expression of the necroptotic pathway is highly restricted in mice (Fig. **EV2A**; (Tabula Muris *et al*, 2018)). Transcript expression of the necroptotic effectors, MLKL and RIPK3, was below detection limits in kidney epithelial, cardiac muscle and resident brain cells, but was frequently detected in progenitor and immune barrier cell populations (Fig. **EV2A**; (Tabula Muris *et al.*, 2018)).

Close inspection of sites where the necroptotic pathway was constitutively expressed showed unexpected layers of spatial regulation (Fig. **2A-B**). In the epithelial barrier of the ileum, Caspase-8 expression was lower in crypts and higher at villi tips, whereas RIPK3 levels peaked in the transit amplifying region and decreased towards the villus tip (Fig. **2Ai, 2Bi**). In the colonic epithelial barrier, both Caspase-8 and RIPK3 exhibited higher expression in the base of the crypt and decreased towards the tip of the crypt (Fig. **2Aii, 2Bii**). It is noteworthy that expression patterns of Caspase-8 and RIPK3 differ between the small and large intestine because these organs exhibit distinct cell death responses to the same inflammatory stimuli (e.g. TNF) or genetic deficiency (e.g. deletion of *Casp8* or *Fadd*) (Bader *et al*, 2023; Schwarzer *et al*, 2020; Tisch *et al*, 2022;

Zelic *et al*, 2018). In liver, Kupffer cells expressed Caspase-8, RIPK1 and RIPK3 (arrowheads Fig. **2Aiii, 2Biii**), whereas hepatocytes expressed Caspase-8 and RIPK1, but not RIPK3. Interestingly, Caspase-8 levels were higher in pericentral hepatocytes than in periportal hepatocytes (arrow Fig. **2Aiii, 2Biii**). Zonation of the necroptotic pathway was also evident in the spleen, with Caspase-8, RIPK1, RIPK3 and MLKL levels peaking in the marginal zone, where circulating antigens are trapped for immune presentation (Fig. **2Aiv, EV2B**). Prior spatial transcriptomics data support the conclusion that necroptotic potential is zoned along the intestinal crypt-to-villus axis (Fig. **EV2C**; (Moor *et al*, 2018)) and along the hepatic central-to-portal axis (Fig. **EV2D**; (Ben-Moshe *et al*, 2019)). We also used spatial transcriptomics on mouse spleen to confirm that necroptotic potential peaks in the marginal zone (Fig. **EV2E-G**).

The expression of RIPK3 appears to be under particularly strict spatial control. For example, in the ileum, RIPK3 levels were high in fast-cycling epithelial progenitors, but low in adjacent, terminally differentiated Paneth cells (open arrowhead Fig. **2Ai**). Published single cell transcriptomics data supports the conclusion that Paneth cells express low levels of RIPK3 under basal conditions (Haber *et al*, 2017). As another example of differential expression, RIPK3 levels were high in fast-cycling colonic epithelial cells, but undetectable in slow-cycling renal epithelial cells (Fig. **1D**). These observations suggest that RIPK3 expression is linked to cell turnover. Indeed, across 103 cell ontologies in the *Tabula Muris* dataset, gene expression of cell cycle markers *Top2a* and *Mki67* correlated with the expression of *Ripk3,* but not *Ripk1* (Fig. **2C** and **EV2A**; (Tabula Muris *et al.*, 2018)). Prior cell cultures studies further suggest that the expression and function of RIPK3 fluctuates during the mitotic cell cycle (Gupta & Liu, 2021; Liccardi *et al*, 2019).

Altogether, by applying a set of optimised immunohistochemistry protocols to multiple organs, we have found that the necroptotic pathway is preferentially expressed at fast-cycling immune barriers under basal conditions. Such targeted expression is

consistent with the evolutionary origin of necroptosis being an anti-pathogen defence measure (Palmer *et al.*, 2021; Petrie *et al.*, 2019; Upton *et al.*, 2010). We further find that necroptotic potential is spatially graded along barriers such as the intestinal mucosa. These gradations in the availability of cell death mediators along barriers likely allow multiple cell death programs to be flexibly deployed against invading pathogens (Cook *et al*, 2014; Doerflinger *et al*, 2020).

Inflammation, dysbiosis or immune challenge trigger local changes in RIPK3 expression

To demonstrate scalability, we used automated immunohistochemistry to characterise the expression of Caspase-8, RIPK1 and RIPK3 across six tissues during TNF-induced Systemic Inflammatory Response Syndrome (SIRS) – a widely-used model of RIPK-dependent pathology (Fig. **3A**; (Duprez *et al*, 2011; Harris *et al*, 2017; Newton *et al.*, 2016; Newton *et al*, 2014; Zelic *et al.*, 2018)). Littermate wild-type mice were intravenously administered TNF~~,~~ or vehicle~~,~~ and tissues were harvested 9 hours later when symptoms such as hypothermia were manifesting (Fig. **3B**). No major changes to Caspase-8 or RIPK1 expression were observed after TNF administration, except for an unidentified population of RIPK1-expressing cells appearing at the onset of apoptosis in lymphoid tissues (Fig. **3C-D**; arrowhead). By comparison, RIPK3 was upregulated in intestinal epithelial cells (Fig. **3E-F**), certain vascular beds (Fig. **3G-H**) and in liver (Fig. **3I-J**); the main sites where RIPK1- and RIPK3-mediated signaling during SIRS has been implicated by knock-in and knockout mouse studies (Duprez *et al.*, 2011; Newton *et al.*, 2016; Zelic *et al.*, 2018). In contrast, RIPK3 levels were not increased in resident cells of the kidney or heart in TNF-treated mice. Our data therefore suggest that targeted upregulation of RIPK3 in resident cells of the gut and liver underlies RIPK-mediated pathology in SIRS. TNF-treatment also changed the pattern of RIPK3 expression in the intestine, potentially

skewing cell death responses in the inflamed gut (Fig. **3E-F**). It was surprising that RIPK3 was detected in peri-portal hepatocytes after TNF administration, given that RIPK3 is epigenetically silenced in hepatocytes under basal conditions (Preston *et al*, 2022). Collectively, our immunohistochemical characterisation of the SIRS mouse model leads us to propose that RIPK3 is regulated akin to a positive acute phase reactant, with hepatic and intestinal–expression that rapidly increases in response to inflammation. In support of this notion, we find that TNF-treatment increased the levels of RIPK3 in serum (Fig. **3K-L**). Moreover, RIPK1-inhibition prevented both TNF-induced hypothermia and the release of RIPK3 into blood (Fig. **3K-L**). These data raise the exciting possibilities that RIPK3 is a novel acute phase reactant, and that circulating levels of RIPK3 are a surrogate measure of RIPK1-mediated signaling.

Next, we addressed whether microbiota-depletion affects necroptotic pathway expression. This question was prompted by studies showing that antibiotics offer protection in various models of intestinal necroptosis (Bader *et al.*, 2023; Gunther *et al*, 2015; Li *et al*, 2020; Xie *et al*, 2020). As shown in Fig. **4A**, a litter of wild-type mice was split into two cages and the water for one cage was supplemented with antibiotics for 6 days. As expected, the cecum of antibiotic-treated mice was enlarged and canonical anti-microbial factors such as lysozyme and REG-3β were reduced in the ileum, but not the spleen, of antibiotic-treated mice (Fig. **4B-C**). These predictable responses to microbiota-depletion also coincided with a lowering of RIPK3 and MLKL gene and protein expression in the ileum, but not the spleen (Fig. **4B-C** and **EV3**). In contrast, Caspase-8 gene and protein expression in the ileum were unaffected by microbiota-depletion, whereas ileal RIPK1 protein levels were increased by antibiotic treatment (Fig. **4B-C** and **EV3**). Similar trends were observed by immunohistochemistry, with epithelial Caspase-8 expression remaining constant, while RIPK1 levels were elevated and RIPK3 expression reduced in the crypt and transit amplifying regions of the ileum in antibiotic-treated mice (Fig. **4D**).

Unexpectedly, immunohistochemistry also showed that microbiota-depletion triggered cytoplasmic accumulations of RIPK1 and RIPK3 in enterocytes at villi tips (Fig. **4D**; arrowheads). These RIPK1^{+} RIPK3^{+} Caspase-8^{-} clusters are unlikely to be necrosomes, as no corresponding phospho-activation of RIPK1 or MLKL was observed (Fig. **EV3**). Instead, these clusters may be due to a microbe-related function, such as lipopolysaccharide handling, that is preferentially performed by enterocytes at villi tips (Berkova *et al*, 2023; Ge *et al*, 2000). These changes to RIPK1/3 could also be related to the reduced epithelial turnover that accompanies microbiota-depletion (Park *et al*, 2016). Overall, we find that expression of the necroptotic pathway responds locally to changes in the microbiome. This response is spatially restricted to the small intestine, zoned along the crypt-to-villus axis, and warrants further investigation given that dysbiosis often occurs in cell death-associated gut disorders such as Crohn's disease (Gevers *et al*, 2014).

Lastly, we used automated immunohistochemistry to uncover a potential non-necroptotic role for RIPK3 in adaptive immunity. We immunised wild-type mice with the model ligand, NP-KLH (4-hydroxy-3-nitrophenylacetyl hapten conjugated to keyhole limpet hemocyanin), and harvested tissues 5 or 14 days later when antigen-specific antibody responses were detectable (Fig. **EV4A**). No changes in the levels or zonation of Caspase-8, RIPK1 or RIPK3 were noted in the ileum of immunised mice and no marked differences in the expression of Caspase-8, RIPK1 or MLKL were observed in the spleen 14 days after immunisation. However, RIPK3 levels were markedly elevated in Ki67^{+} germinal centres (arrowheads Fig. **EV4B**). This finding suggests that RIPK3 may have a non-necroptotic role in antibody production. To investigate this possibility, *Ripk3*$^{+/+}$ and *Ripk3*$^{-/-}$ littermate mice were immunised with NP-KLH and humoral immune responses were measured in blood and spleen (Fig. **EV4C-J**). RIPK3-deficiency did not alter the circulating levels of antigen-specific antibodies 5 days after immunisation (Fig. **EV4C-D**). Similarly, RIPK3-deficiency did not influence the number of class-switched B cells in the spleen (Fig. **EV4E-**

F), the number of antigen-specific plasma cells in the spleen (Fig. EV4G), or the amount of circulating antigen-specific antibodies 14 days after immunisation (Fig. EV4H-J). Thus, consistent with prior studies (Newton *et al*, 2004), RIPK3 does not overtly affect early antigen-specific antibody responses. Future studies should explore a role of RIPK3 in splenic germinal centres, especially given that RIPK3 has a mechanistically undefined non-necroptotic role during lymphoproliferative disease (Alvarez-Diaz *et al*, 2016).

In summary, by employing a toolbox of automated immunohistochemical stains, we find that expression of the necroptotic pathway, in particular RIPK3, is responsive to inflammation, dysbiosis or immunisation. These context-specific changes are tightly regulated across space and time, underscoring the need for robust, scalable, *in situ* assays to pinpoint necroptotic pathway expression and activation.

Automated immunohistochemical detection of the human necroptotic pathway

Important differences exist between the human and mouse necroptotic pathways (Chen *et al*, 2013; Davies *et al*, 2020; Horne *et al*, 2023; Petrie *et al*, 2018; Samson *et al.*, 2021b; Sun *et al.*, 2012; Tanzer *et al*, 2016). For instance, the primary sequence of RIPK3 and MLKL are poorly conserved between species (Horne *et al.*, 2023), and humans uniquely express Caspase-10 which likely negates necroptotic signaling (Ramirez & Salvesen, 2018; Tanzer *et al*, 2017). Thus, in parallel to developing assays for the murine necroptotic pathway, seventeen antibodies against Caspase-8, Caspase-10, RIPK1, RIPK3 or MLKL were tested on wild-type versus knockout formalin-fixed paraffin-embedded HT29 human cells via immunoblot, and then iteratively optimised for immunohistochemistry (see *Methods* and Fig. EV5). While Caspase-10 remained refractory to immunohistochemical detection, six automated immunohistochemistry protocols were developed for human Caspase-8, RIPK1, RIPK3 or MLKL (Fig. EV5).

These immunohistochemistry protocols detected diffuse cytoplasmic signals for Caspase-8, RIPK1, RIPK3 and MLKL in cells under resting conditions (Fig. **5**), and in cells undergoing-TNF-induced apoptosis (via co-treatment with TNF (T) and a Smac mimetic (S); Fig. **5**). Conversely, immunohistochemistry detected intracellular clusters of Caspase-8, RIPK1, RIPK3 or MLKL in cells undergoing TNF-induced necroptosis (via co-treatment with T and S and the caspase inhibitor IDN-6556 (I); arrowhead Fig. **5**). These intracellular clusters are presumed to be necrosomes because they resemble prior images of necrosomes (Chen *et al.*, 2022b; Samson *et al.*, 2021a; Samson *et al.*, 2020; Sun *et al.*, 2012) and because orthogonal approaches show that Caspase-8, RIPK1, RIPK3 and MLKL are recruited to necrosomes during TNF-induced necroptosis (de Almagro *et al*, 2017; He *et al.*, 2009; Li *et al*, 2021; Sun *et al.*, 2012). Notably, the translocation of Caspase-8 and RIPK1, but not MLKL, to necrosomes could also be detected in mouse dermal fibroblasts undergoing TNF-induced necroptosis (Fig. **EV6**). This species-dependent difference is likely due to dissimilarities in the interaction between RIPK3 and MLKL, which is thought to be more transient in mouse than in human cells (Petrie *et al.*, 2018). Next, by combining automated immunohistochemistry with high-resolution digital slide scanning (~250nm resolution) and customised image segmentation, we show that necrosomes can be detected and quantified across a large population of cells in an unbiased manner (Fig. **5B-C**). We observed that the accuracy of segmenting human Caspase-8 or MLKL at necrosomes is higher than that of RIPK1, because the small puncta formed by necrosomal RIPK1 are near the resolution limit of existing brightfield slide scanners (Fig. **5C**). Nonetheless, since necrosomes are a pathognomonic feature of necroptotic signaling, we propose that machine-based detection of necrosomes could be developed into a diagnostic assay for pinpointing necroptosis in formalin-fixed human patient biopsies. This proposal assumes that immunostaining protocols developed on cell pellets retain their specificity when applied to tissues. To test this assumption, we used two

antibodies - one specific for mouse RIPK3 and one specific for human RIPK3 - on spleens from *Ripk3*$^{-/-}$ mice, *Ripk3*$^{+/+}$ mice or knock-in mice expressing human RIPK3 (see *Methods*). As shown in Fig. **EV7**, immunoblotting and immunohistochemistry with the respective antibodies accurately discriminated between the expression of mouse RIPK3 or human RIPK3 in spleen. These data suggest that immunohistochemistry protocols optimised on cell pellets can also be used to specifically stain tissues.

Necrosome immunodetection in patients with IBD

Ulcerative colitis (UC) and Crohn's disease (CD) are the main types of IBD (Kobayashi *et al*, 2020; Roda *et al*, 2020). The causes of adult onset IBD are multifactorial (Ananthakrishnan, 2015; Graham & Xavier, 2020). While many studies show that excess necroptosis promotes IBD-like pathology in mice (Gunther *et al.*, 2011; Matsuzawa-Ishimoto *et al*, 2017; Schwarzer *et al.*, 2020; Vlantis *et al*, 2016; Wang *et al*, 2020a; Xie *et al.*, 2020; Xu *et al*, 2023), few studies have examined the prevalence of necroptosis in IBD patients (Negroni *et al*, 2017; Pierdomenico *et al*, 2014; Shi *et al*, 2020). One Phase II trial of a RIPK1 inhibitor in UC has failed to demonstrate clinical efficacy (Weisel *et al*, 2021), but several other clinical and preclinical trials of RIPK1 inhibitors in IBD are underway. Thus, the role of necroptosis in IBD requires further investigation. We collected intestinal biopsies from adults with UC, CD and non-IBD patients (Fig. **6A** together with clinical information in Table **1**). To capture the chronology of disease, biopsies were collected from endoscopically 'non-inflamed', 'marginally inflamed' and 'inflamed' intestinal tissue from patients with IBD. The grading of inflammation was verified by blinded histopathology scores (Fig. **6B**). Cell death signaling in biopsies from each location and endoscopic grade was assessed by immunoblot (Fig. **6C** and Table **1**). To assist interpretation, patient samples (blue annotations in Fig. **6C**) were immunoblotted alongside lysates from HT29 cells undergoing apoptosis or necroptosis (red annotations in Fig. **6C**). Apoptotic signaling

was inferred from increases in the conversion of pro-Caspase-3, -8 and -10 into their active cleaved forms (open arrowheads in Fig. **6C**). Necroptotic signaling was inferred from increases in the abundance of phosphorylated RIPK3 and MLKL, relative to their non-phosphorylated forms (asterisks in Fig. **6C**). This approach showed that cell death signaling is elevated in intestinal tissue from patients with IBD relative to patients without IBD, especially in inflamed intestinal biopsies from IBD patients (Fig. **6C** and **EV8**). However, marked heterogeneity in the prevailing form of cell death was apparent in both UC and CD patients; with apoptosis dominant in some IBD cases (patients B and F in Fig. **6C** and patient I in Fig. **EV8**), and necroptosis dominant in others (patients D and H in Fig. **6C**). Given the ongoing development of RIPK1 inhibitors, it is noteworthy that phosphorylated MLKL coincided with phosphorylated RIPK1 in some, but not all patients with IBD (patients D versus H in Fig. **6C**). Why cell death mechanisms vary between patients is currently unknown. Collectively, we find that cell death signaling increases in the inflamed gut, supporting the idea that cell death inhibitors are a potential treatment option for IBD. Whether apoptosis or necroptosis manifests in an individual IBD patient appears to be highly variable, highlighting the need for diagnostic approaches, such as automated immunohistochemistry, to identify patients who may benefit from anti-necroptotic therapy.

Having identified biopsies with differing modes of intestinal cell death, we next applied our panel of automated immunohistochemical stains to matched biopsies (collected from the same patients at the same time and from the same location; Table 1; note that a biopsy for immunohistochemistry was not collected from patient F). Consistent with immunoblotting data showing increased apoptosis in patients B and I (Fig. **6C** and **EV8**), immunohistochemistry detected substantially more cleaved Caspase-3^{+} epithelial cells in patients B and I (open arrowheads Fig. **EV9** and **EV10**) compared to other patients in the cohort. No obvious changes to epithelial RIPK1, RIPK3 and MLKL were evident

between patients (Fig. **EV9** and **EV10**). By comparison, cytoplasmic clusters of Caspase-8 were evident in the epithelial layer of the inflamed biopsy from patient D and H (closed arrowheads in **Fig. 6D,** closed arrowheads in **EV9** and **EV10**). Since these cytoplasmic clusters of Caspase-8 were reminiscent of the Caspase-8^{+} necrosomes in necroptotic HT29 cells (**Fig. 5**), we used the same high-resolution digital slide scanning and unbiased image segmentation approach as before. This quantitation showed that the number of intraepithelial Caspase-8^{+} clusters was low in non-IBD patient C and increased with inflammation in IBD patient D (**Fig. 6E**). This trend mirrors the levels of necroptotic signaling in IBD patient D (**Fig. 6B**), suggesting that cytoplasmic clusters of Caspase-8^{+} may represent bona fide necrosomes. Why the immunohistochemical detection of Caspase-8 distinguishes between necroptosis and apoptosis is unclear, but this likely relates to the observation that Caspase-8-containing complexes that form during necroptosis are qualitatively different to those that form during apoptosis (de Almagro *et al.*, 2017). This case study suggests that automated immunohistochemical detection of Caspase-8^{+} clusters in patient biopsies is feasible and could be developed into a diagnostic assay for pinpointing necroptosis in clinical practice. To this end, future studies with a larger number of biopsies are needed to determine whether the immunoblot detection of necroptotic signaling significantly correlates with the immunohistochemical detection of Caspase-8^{+} clusters.

Discussion:

The difficulty of reliably detecting necroptotic signaling in fixed tissues has been a longstanding issue, generating confusion and conflicting results in the literature. To address this problem, we optimised the immunohistochemical detection of Caspase-8, RIPK1, RIPK3 and MLKL in formalin-fixed paraffin-embedded samples. While our prior studies immunostained non-crosslinked fixed monolayers (Samson *et al.*, 2021a; Samson *et al.*, 2020), here we used formalin-fixed paraffin-embedded specimens consistent with standard practice in clinical pathology and research departments around the world. In total, over 300 different immunostaining conditions were tested, yielding 13 automated immunohistochemistry protocols that we anticipate will be of broad utility to the cell death community and drive new insight into the causes, circumstances, and consequences of necroptosis. To assess the reliability of our automated protocols, we benchmarked our immunostaining results against data obtained using other methodologies. For instance, our automated immunohistochemistry protocols produced results that were comparable to public resources generated using proteomic, single cell transcriptomic, and spatial transcriptomic approaches (Ben-Moshe *et al.*, 2019; Geiger *et al*, 2013; Moor *et al.*, 2018; Tabula Muris *et al.*, 2018). Confidence was also taken from the similar staining patterns produced between three Caspase-8 antibodies (clones D53G2, 3B10 and 1G12), between two RIPK3 antibodies (clones 8G7 and 1H12), and between mouse and human intestinal tissue using the same RIPK1 antibody (clone D94C12). Thus, multiple lines of evidence suggest that the automated protocols described herein are specific and sensitive.

Our approach for optimising and interpreting immunohistochemical signals relied upon quantitative analyses that carries important technical considerations. First and foremost, the signals produced by immunohistochemistry are non-linear (Bobrow & Moen, 2001). Moreover, before quantitation, we digitally unmixed immunosignals from the haematoxylin counterstain, which is another non-linear transformation of signal intensity

(Landini *et al*, 2021). Thus, only relative changes in expression levels were inferred from changes in immunohistochemical signal intensity. Because of this caveat, we only compared and quantified immunosignals between closely matched specimens, such as corresponding wild-type and knockout samples where both samples were sectioned at the same time, mounted on the same slide, and stained and imaged contemporaneously. To aid quantitation, all our immunohistochemistry protocols were developed to produce unsaturated signals. One final salient point is that this study used automated embedding and immunostaining procedures, with all quantification using macros that analyse a high number (typically thousands) of cells per sample. Thus, the automated immunohistochemistry protocols described herein can be used for quantitative purposes, but only when comparing closely matched specimens, and ideally with supporting data from alternative methodologies such as spatial transcriptomics. These recommendations reduce, but do not eliminate, the need to use knockout samples as a control for specificity.

The phosphorylated forms of RIPK1, RIPK3 and MLKL are the most widely used markers of necroptotic signaling (Horne *et al.*, 2023). Accordingly, prior attempts to detect necroptotic signaling in fixed specimens have focussed on phospho-RIPK1, -RIPK3 and -MLKL (Dominguez *et al.*, 2021; He *et al*, 2021; Li *et al.*, 2017; Li *et al*, 2022; Rodriguez *et al*, 2022; Rodriguez *et al.*, 2016; Samson *et al.*, 2021a; Samson *et al.*, 2020; Wang *et al.*, 2014; Webster *et al.*, 2018; Zhang *et al.*, 2020). However, there are drawbacks with this approach: 1) antibodies against phosphorylated epitopes in RIPK1/3 and MLKL exhibit much poorer signal-to-noise properties than do antibodies against unphosphorylated epitopes in RIPK1/3 and MLKL (Samson *et al.*, 2021a); 2) while knockout samples are sufficient for verifying non-phospho-signals, multiple controls are needed to authenticate phospho-signals (e.g. resting, knockout and phosphatase pre-treated samples); and 3) because only a small fraction of RIPK1/3 and MLKL is phosphorylated during necroptosis these phospho-species are inherently more difficult to detect than their unphosphorylated

counterparts. Indeed, as is standard practice when detecting necroptosis via immunoblot, the immunohistochemical detection of phospho-RIPK1, -RIPK3 and -MLKL can only be interpretated when their unphosphorylated forms can also be detected. For these reasons, we focused on the immunohistochemical detection of unphosphorylated RIPK1, RIPK3 and MLKL, and used the immunodetection of necrosomes as a marker of necroptotic signaling.

It was surprising that expression of the necroptotic pathway was heavily restricted under steady-state conditions in mice. That fast-cycling progenitors and immune barrier cells are the dominant expressors of RIPK3 and/or MLKL suggests that the existential role of necroptosis is to protect the host from invading pathogens. The phenotypes and cell types affected in mice carrying activation-prone polymorphisms in *Mlkl* also supports the view that the ancestral role of necroptosis lies in innate immunity (Garnish *et al*, 2023; Hildebrand *et al*, 2020; Zhu *et al*, 2022). The absence of necroptotic pathway expression in slow-cycling cell populations was equally striking, with RIPK3 and/or MLKL undetectable in resident cells of the heart (except for certain fibroblasts), the brain (except for leptomeningeal vessels), the kidney and the liver (except for Kupffer cells) in mice under basal conditions. These observations challenge a vast body of literature, highlighting the need for robust well-controlled methodologies. These results lead us to propose that slow-cycling cell populations ensure longevity by avoiding inadvertent necroptotic signaling. The observation that RIPK3 expression is rapidly derepressed in hepatocytes during inflammation supports the notion that long-lived cells actively suppress necroptotic signaling, but only in the absence of challenge. The derepression of RIPK3 may reconcile the contribution of necroptosis in inflammatory disorders such as hepatocellular carcinoma (Vucur *et al*, 2023), acute myocardial infarction (Luedde *et al.*, 2014), acute ischemic stroke (Degterev *et al*, 2005) and kidney ischemia-reperfusion injury (Linkermann *et al.*, 2013). Notably, the Human Protein Atlas lacks immunohistochemical data for RIPK3 and

MLKL, and therefore it remains unknown whether the necroptotic pathway is similarly restricted in humans (Uhlen *et al*, 2015).

It is noteworthy that certain non-mitotic cells, such as bone marrow-derived macrophages, are highly sensitive to necroptotic stimuli (Zelic & Kelliher, 2018). Thus, necroptosis is not reliant upon mitosis. Nonetheless, given the striking correlation between RIPK3 and mitotic marker expression, and since RIPK3's activity and interactome vary considerably during the cell cycle (Gupta & Liu, 2021; Liccardi *et al.*, 2019), future studies should investigate how cell proliferation influences necroptotic susceptibility.

To exemplify the utility of our approach, we applied our full immunohistochemistry panel to determine whether inflammation, dysbiosis or immunisation alter necroptotic pathway expression in mice. Each of these challenges altered necroptotic pathway expression in a manner that chiefly involved local shifts in RIPK3 expression. This profiling of the necroptotic pathway yielded many unexpected observations, including: 1) RIPK3 expression is disinhibited in hepatocytes after TNF administration, with contemporaneous increases in circulating RIPK3 levels; 2) RIPK3 expression is suppressed in the gut during antibiotic administration with RIPK1/3 coalescing into unidentified cytoplasmic clusters in epithelial cells at the villus tip; and 3) RIPK3 expression is uniquely upregulated in splenic germinal centres after immunisation. While the mechanistic basis for these findings warrants future attention, their initial description here illustrates the benefits of studying the necroptotic pathway using automated immunohistochemistry, and raises questions about whether RIPK3 expression is also regulated similarly in humans. This line of enquiry circles back to the idea that variations in RIPK3 expression are a key determinant of necroptotic potential (Cook *et al.*, 2014; He *et al.*, 2009; Najafov *et al*, 2018).

Our data raise the possibility that the immunodetection of intracellular Caspase-8^{+} clusters necrosomes could be used as an *in situ* marker of necroptotic signaling in IBD patients. To reach this conclusion, we developed a suite of automated

immunohistochemical protocols to detect the relocation of necroptotic effectors into necrosomes and validated the presence of necroptotic signaling in closely matched biopsies from patients with IBD using immunoblot. Collectively, these experiments show that intracellular clusters of Caspase-8, RIPK1, RIPK3, and MLKL are readily detectable under idealised cell culture conditions, that elevated necroptotic signaling occurs in a subset of IBD, and that cytoplasmic clustering of Caspase-8 correlated with necroptotic signaling across a set of biopsies from two patients with IBD. Why clusters of Caspase-8, but not clusters of RIPK1 or MLKL, were detectable in biopsies with active necroptotic signaling is unknown but may be due to technical limitations (e.g. resolution limit) or gaps in our understanding of how necroptosis manifests *in vivo*. Another important issue is whether the immunohistochemical detection of Caspase-8^{+} clusters can be used to quantify necroptotic signaling in larger cohorts of patients with IBD and in patients with other clinical indications. Notwithstanding these issues, the detection of *in situ* changes in necroptotic pathway expression in a scalable, quantitative, and automated manner represents a major leap forward in the capacity to pinpoint when and where necroptosis arises in both health and disease.

Materials and Methods:

Materials

Primary antibodies were rat anti-mouse Caspase-8 (clone 3B10; RRID:AB_2490519; 1g/L produced in-house (O'Reilly *et al*, 2004) and available from AdipoGen Cat#AG-20T-0138), rat anti-mouse Caspase-8 (clone 1G12; RRID:AB_2490518; 1g/L produced in-house (O'Reilly *et al.*, 2004) and available from AdipoGen Cat#AG-20T-0137), rabbit anti-Caspase-8 (clone D35G2; RRID:AB_10545768; Cell Signaling Technology Cat#4790), rabbit anti-phospho-RIPK1 (clone D813A; RRID:AB_2799268; Cell Signaling Technology Cat#44590S), mouse anti-RIPK1 (clone 38/RIP; RRID:AB_397831; 0.25g/L BD Biosciences Cat#610459), mouse anti-RIPK1 (clone 334640; RRID:AB_2253447; 0.5g/L; R&D Systems Cat#MAB3585), rabbit anti-RIPK1 (clone D94C12; RRID:AB_2305314; Cell Signaling Technology Cat#3493), rabbit anti-RIPK3 (clone 18H1L23; RRID: AB_2866471; 0.5g/L; Thermo Fisher Scientific Cat#703750), rabbit anti-phospho-RIPK3 (clone D6W2T; RRID:AB_2800206; Cell Signaling Technology Cat#93654), rat anti-RIPK3 (clone 1H12; 2g/L produced in-house (Samson *et al.*, 2021a)), rat anti-RIPK3 (clone 8G7; RRID: RRID:AB_2940810; 2g/L produced in-house (Petrie *et al.*, 2019) and available from Millipore Cat#MABC1595), rabbit anti-phospho-MLKL (clone D6E3G; RRID:AB_2799112; Cell Signaling Technology Cat# 37333), rabbit anti-phospho-MLKL (clone EPR9514; RRID:AB_2619685; Abcam Cat#ab187091; (Wang *et al.*, 2014)), mouse anti-MLKL (clone 3D4C6; RRID:AB_2882029; 1.957g/L; Proteintech Cat#66675-1-IG), rabbit anti-mouse MLKL (clone D6W1K; RRID:AB_2799118; Cell Signaling Technology Cat#37705), rat anti-mouse MLKL (clone 5A6; RRID:AB_2940800; 50g/L produced in-house (Samson *et al.*, 2021a) and available from Millipore Cat#MABC1634), rat anti-MLKL (clone 3H1; RRID:AB_2820284; 2g/L produced in-house (Murphy *et al.*, 2013) and available from Millipore Cat# MABC604), mouse anti-Caspase-10 (clone 4C1; RRID:AB_590721; 1g/L; MBL International Cat# M059-3), mouse anti-Caspase-8 (clone B.925.8;

RRID:AB_10978471; 0.619g/L Thermo Fisher Scientific Cat# MA5-15226), mouse anti-Caspase-8 (clone 5D3; RRID:AB_590761; 1g/L; MBL International Cat#M058-3), rat anti-human RIPK3 (clone 1H2; RRID:AB_2940816; 2g/L produced in-house (Petrie *et al.*, 2019) and available from Millipore Cat# MABC1640), rabbit anti-human RIPK3 (clone E1Z1D; RRID:AB_2687467; Cell Signaling Technology Cat# 13526), rabbit anti-human RIPK3 (clone E7A7F; RRID:AB_2904619; Cell Signaling Technology Cat# 10188), rat anti-human MLKL (clone 7G2; RRID:AB_2940818; 2g/L produced in-house (Samson *et al.*, 2020) and available from Millipore Cat# MABC1636), rat anti-human MLKL (clone 10C2; RRID:AB_2940821; 2g/L produced in-house (Samson *et al.*, 2020) and available from Millipore Cat# MABC1635), rabbit anti-MLKL (clone 2B9; RRID:AB_2717284; 1g/L; Thermo Fisher Scientific Cat#MA5-24846), rabbit anti-MLKL (clone EPR17514; RRID:AB_2755030; 1.9g/L; Abcam Cat# ab184718), mouse anti-GAPDH (clone 6C5; RRID:AB_2107445; 1g/L; Millipore Cat# MAB374), rabbit anti-smooth muscle actin (clone D4K9N; RRID:AB_2734735; Cell Signaling Technology Cat#9245S), rabbit anti-lysozyme (clone EPR2994(2); RRID:AB_10861277; Abcam Cat#108508), cleaved-caspase 3 (Cell Signaling Technology, #9661), Ki67 (Cell Signaling Technology, #12202). The concentration of antibodies from Cell Signaling Technology is often not provided and thus was not listed here.

Secondary antibodies for immunoblotting were horseradish peroxidase (HRP)-conjugated goat anti-rat immunoglobulin (Ig) (Southern BioTech Cat#3010-05), HRP-conjugated goat anti-rabbit Ig (Southern BioTech Cat#4010-05) and HRP-conjugated goat anti-mouse Ig (Southern BioTech Cat#1010-05).

Reagents for immunohistochemistry were HRP-conjugated anti-rabbit Ig (Agilent Cat# K400311-2), HRP-conjugated anti-mouse Ig (Agilent Cat# K400111-2), MACH4 universal

HRP-Polymer (Biocare Medical Cat#M4U534L), ImmPRESS HRP-conjugated anti-rat IgG for human samples (Vector Laboratories CatcVEMP740450), HRP-conjugated anti rat IgG for mouse samples (R&D Systems Cat#VC005-125), Rabbit Linker (Agilent Cat#GV80911-2). Epitope Retrieval Solution 1 (Leica Cat#AR9961), Epitope Retrieval Solution 2 (Leica Cat#AR9640), Retrieval Solution Low pH (Agilent Cat#GV80511-2), Retrieval Solution High pH (Agilent Cat#GV80411-2), 3,3'-diaminobenzidine (DAB) substrate (Agilent Cat#GV82511-2 or GV92511-2), Dako REAL Peroxidase-blocking reagent (Agilent S202386-2), bluing reagent (Leica, 3802915), Background Sniper (Biocare Medical Cat#BS966L), Dako Protein Block (Agilent Cat#X0909), 'Normal' block (Agilent Cat#S202386-2), EnVision FLEX TRS High pH (Agilent Cat# GV80411-2), EnVision FLEX TRS Low pH (Agilent Cat# GV80511-2), MACH4 universal HRP polymer (Biocare Medical Cat#M4U534L), and DPX (Trajan Cat#EUKITT), Opal TSA-Dig (Akoya Cat#OP-001007), Opal Polaris 780 reagent (Akoya Cat#OP-001008), and HRP-conjugated anti-digoxigenin antibody (Cell Signaling Technology, clone D8Q9J, Cat#49620).

Mice, research ethics and housing

All experiments were approved by The Walter and Eliza Hall Institute (WEHI) Animal Ethics Committee, Australia, in accordance with the Prevention of Cruelty to Animals Act (1986), with the Australian National Health and Medical Research Council Code of Practice for the Care and Use of Animals for Scientific Purposes (1997), and with the ARRIVE guidelines (Percie du Sert *et al*, 2020). Mice were housed at the WEHI animal facility under specific pathogen-free, temperature- and humidity-controlled conditions and subjected to a 12 h light/dark cycle with ad libitum feeding. Mice without functional MLKL alleles (*Mlkl*$^{-/-}$) have been described previously (Murphy *et al.*, 2013). Mice without functional RIPK3 alleles (*Ripk3*$^{-/-}$) have been described previously (Tovey Crutchfield *et al*, 2023). Mice without functional alleles of RIPK1, RIPK3 and Caspase-8 (*Ripk1*$^{-/-}$

585 *Ripk3*$^{-/-}$*Casp8*$^{-/-}$ triple knockout mice) and *Ripk3*$^{-/-}$*Casp8*$^{-/-}$ double knockout mice have
586 been described previously (Rickard *et al*, 2014) and were derived from reported mouse
587 strains (Kelliher *et al*, 1998; Newton *et al.*, 2004; Salmena *et al*, 2003). Human RIPK3
588 knock-in mice in which the human RIPK3 coding sequence was inserted into the mouse
589 *Ripk3* locus of C57BL/6J mice were provided by Anaxis Pharma Pty Ltd.
590
591 **Mouse tissue lysate preparation**
592 Mouse tissues were homogenised with a stainless steel ball bearing in a Qiagen
593 TissueLyzer II (30 Hz, 1min) in ice-cold RIPA buffer (10mM Tris-HCl pH 8.0, 1mM EGTA,
594 2mM MgCl2, 0.5% v/v Triton X100, 0.1% w/v sodium deoxycholate, 0.5% w/v sodium
595 dodecyl sulfate (SDS) and 90mM NaCl) supplemented with 1x Protease & Phosphatase
596 Inhibitor Cocktail (Cell Signaling Technology Cat#5872) and 100 U/mL Benzonase (Sigma-
597 Aldrich Cat#E1014). 1mL of RIPA buffer per 25mg of tissue was used for homogenisation.
598
599 **Immunoblot**
600 For Fig. **EV1**, **EV5** and **EV7**, RIPA lysates were boiled for 10min in Laemmli sample buffer
601 (126 mM Tris-HCl, pH 8, 20% v/v glycerol, 4% w/v sodium dodecyl sulfate, 0.02% w/v
602 bromophenol blue, 5% v/v 2-mercaptoethanol) and fractionated by 4-15% Tris-Glycine gel
603 (Bio-Rad Cat#5678084) using Tris-Glycine running buffer (0.2M Tris-HCl, 8% w/v SDS,
604 0.15M glycine). After transfer onto nitrocellulose, membranes were blocked in 1% w/v
605 bovine serum albumin (BSA; for Caspase-8 antibody clone B.925.8) or 5% w/v skim cow's
606 milk (for all other antibodies) in TBS+T (50mM Tris-HCl pH7.4, 0.15M NaCl, 0.1 v/v
607 Tween20), probed with primary antibodies (1:2000 dilution for rat primary antibodies or
608 1:1000 for other primary antibodies in the above blocking buffers; supplemented with
609 0.01% w/v sodium azide; see *Materials* above) overnight at 4°C, washed twice in TBS+T,
610 probed with an appropriate HRP-conjugated secondary antibody (see *Materials* above),

washed four times in TBS+T and signals revealed by enhanced chemiluminescence (Merck Cat#WBLUF0100) on a ChemiDoc Touch Imaging System (Bio-Rad). Between probing with primary antibodies from the same species, membranes were incubated in stripping buffer (200 mM glycine pH 2.9, 1% w/v SDS, 0.5 mM TCEP) for 30 min at room temperature then re-blocked.

For Fig. 4, 6, EV3, and EV8, RIPA lysates were boiled for 10min in Laemmli sample buffer (126 mM Tris-HCl, pH 8, 20% v/v glycerol, 4% w/v SDS, 0.02% w/v bromophenol blue, 5% v/v 2-mercaptoethanol) and fractionated by 4–12% Bis-Tris gel (Thermo Fisher Scientific Cat#NP0335BOX) using MES running buffer (Thermo Fisher Scientific Cat#NP000202). After transfer onto polyvinylidene difluoride (Merck Cat# IPVH00010), gels were Coomassie-stained as per manufacturer's instructions (Thermo Fisher Scientific Cat#LC6060) and membranes were blocked in 5% w/v skim cow's milk in TBS+T and then probed as above.

Mouse tissue fixation

Tissues were immediately harvested after euthanasia and placed in 10% v/v Neutral Buffered Formalin (NBF) (Confix Green; Australian Biostain Cat#AGFG.5L). A ratio of one part tissue to >10 parts formalin was used. Unless stipulated, tissues were incubated in formalin at room temperature for 24-72 hours.

Paraffin embedding, microtomy and immunostaining

Unless stipulated, formalin-fixed cells/tissues were paraffin embedded using the standard 8 hour auto-processing protocol of the Tissue-Tek VIP® 6 AI Tissue Processor (Sakura Finetek USA). Paraffin embedded cells/tissues were cut in 4µm-thick sections onto adhesive slides (Menzel Gläser Superfrost PLUS). Haematoxylin and eosin staining was

done on the Autostainer XL (Leica ST5010). Immunohistochemistry was performed on an automated system: the Bond RX (Leica) or the DAKO OMNIS (Agilent). While the automated immunohistochemistry protocols used in this manuscript are fully stipulated in File **EV1**, a brief overview of these methods is as follows: Step 1 was deparaffinisation (Phase 1: Clearify Clearing Agent; Phase 2: deonised water), Step 2 was heat-induced antigen retrieval (EnVision FLEX TRS, High pH or Low pH retrieval buffer. Treatment time was antibody-dependent), Step 3 was endogenous peroxidase blocking (Dako REAL Peroxidase-blocking reagent. Incubation time was antibody-dependent), Step 4 was protein blocking (Background Sniper, Dako Protein Block or Normal block. Incubation 10 minutes), Step 5 was primary antibody incubation (dilutions and incubation times were antibody-dependent), Step 6 was option signal amplification (amplification technique was antibody-dependent. Rabbit linker. Incubation 15 minutes), Step 7 was secondary reagent with horseradish peroxidase (anti-rabbit HRP polymer, anti-mouse HRP polymer, MACH4 universal HRP polymer, ImmPRESS anti-rat HRP polymer, anti-rat HRP polymer and in-house HRP signal amplification detection. Reagent and incubation was antibody-dependent), Step 8 was signal detection (chromogen-substrate DAB. Onboard mixing and incubation 10 minutes), Step 9 was counterstaining (in-house made Mayer's Haematoxylin for 1 minute followed by Bluing reagent for 1 minute), Step 10 was dehydration, mounting in DPX and coverslipping using Leica CV5030 platform.

Image acquisition

Unless stipulated, slides were scanned on: 1) 3D Histech Pannoramic Scan II (objective: magnification 20x, numerical aperture 0.8, media dry; software: Pannoramic SCAN 150 1.23 SP1 RTM and SlideViewer 2.8.178749), or 2) Olympus VS200 (objective: 20x, numerical aperture 0.8, media dry; software: Olympus VS200 ASW 3.41). Where higher

resolution was required, slides were scanned on the Olympus VS200 using the 60x objective (numerical aperture 1.42, media oil).

Post-acquisition processing of displayed micrographs

All displayed micrographs were acquired with VS200 Research Slide Scanner (Olympus). Representative full-resolution 8-bit RGB micrographs of the WT and KO tissues/cells were imported into ImageJ 1.53t (Schindelin *et al*, 2012). Brightness-and-contrast was adjusted to 0-235 units and then gamma levels adjusted by 1-2.5-fold. Capture settings and post-acquisition image transformations were held constant between any micrographs that were being compared.

Immunohistochemistry signal-to-noise ratio (S/N) analysis

Sections of wild-type (WT) and corresponding knockout (KO) tissues/cells on the same slide were immunostained and imaged. Representative full-resolution 8-bit RGB micrographs of the WT and KO tissues/cells were imported into ImageJ 1.53t (Schindelin *et al.*, 2012) and the 'H-DAB' function of the 'Colour Deconvolution 2' plugin (Landini *et al.*, 2021) was used to unmix the DAB and hematoxylin channels. A dilated mask of the auto-thresholded hematoxylin channel was applied to the corresponding DAB channel to select an area-of-interest, and then a histogram of pixel intensities from the DAB channel for both the WT and KO micrographs was determined. The 'WT histogram' was then divided by the 'KO histogram' to yield a S/N curve (see Fig.**1A** for example). A weighted integral of the S/N curve was calculated as a numerical index of specificity (red box in Fig. **1A**). The representative micrographs used to calculate S/N curves were of equivalent size, included >1000 cells per sample and their gamma levels unchanged.

Quantitation of zonation via immunohistochemistry

Representative full-resolution 8-bit RGB micrographs of the WT tissues were imported into ImageJ 1.53t (Schindelin *et al.*, 2012). Brightness-and-contrast was adjusted to 0-235 units and the 'H-DAB' function of the 'Colour Deconvolution 2' plugin (Landini *et al.*, 2021) was used to unmix the DAB and hematoxylin channels. The look-up-table for the DAB channel was converted to grayscale and pixel values inverted. The 'Segmented Line tool' was used to draw a line (27.4µm wide to approximate 2 cell widths) along the main axis of the following zones: 1) crypt base to villi tip in the ileum, 2) crypt base to crypt tip in the colon, 3) peri-central hepatocytes to peri-portal hepatocytes, and 4) white matter to red pulp in the spleen. The 'Plot Profile tool' was used to quantify the immunosignal along the drawn axis, which was then averaged across N=10-20 representative zones per mouse.

Quantitation of endothelial RIPK3 levels via immunohistochemistry

Sections were subjected to automated immunohistochemistry for smooth muscle actin (SMA) and RIPK3 (see File **EV1**). SMA signals were detected with a brown DAB product. RIPK3 signals were detected with a pink DAB product. Sections were not counterstained with hematoxylin. Full-resolution 8-bit RGB micrographs (taken with 60x objective; Olympus VS200) were imported into Image J 1.53t (Schindelin *et al.*, 2012) and endothelial RIPK3 levels analysed using a custom semi-automated macro in a non-blinded manner. In brief, cross-sections of individual SMA^+ vessels were chosen, SMA and RIPK3 signals were unmixed using the 'Colour Deconvolution 2' plugin (Landini *et al.*, 2021). An auto-thresholded mask of the SMA^+ intima was then used to segment the endothelial area. The total RIPK3 signal in this endothelial area was expressed per unit area. This procedure was repeated for N=50 vessels per mouse.

Quantitation of hepatocyte RIPK3 levels via immunohistochemistry

Sections were subjected to automated immunohistochemistry for RIPK3 (see File **EV1**). RIPK3 signals were detected with brown DAB product and sections were counterstained with hematoxylin. Representative full-resolution 8-bit RGB micrographs (taken with the 60x objective; Olympus VS200) were imported into Image J 1.53t (Schindelin *et al.*, 2012) and RIPK3 levels within individual hepatocytes analysed using a custom fully-automated macro. In brief, haematoxylin-stained nuclei were unmixed from the RIPK3 signal using the 'Colour Deconvolution 2' plugin (Landini *et al.*, 2021). Nuclei were segmented using the 'Analyze Particles' function of Image J and hepatocyte nuclei distinguished from Kupffer cell nuclei on the basis of their larger size and circularity. The total RIPK3 signal in the cytosolic area surrounding hepatocyte nuclei was segmented, measured and expressed per unit area. N=90 hepatocytes per mouse were measured.

Quantitation of Kupffer cell RIPK3 levels via immunohistochemistry

Sections were subjected to automated immunohistochemistry for RIPK3 (see File **EV1**). RIPK3 signals were detected with brown DAB product and sections counterstained with hematoxylin. Representative full-resolution 8-bit RGB micrographs (taken with the 60x objective; Olympus VS200) were imported into Image J 1.53t (Schindelin *et al.*, 2012) and RIPK3 levels within individual Kupffer cells were analysed using a custom fully-automated macro. In brief, the RIPK3 signal was unmixed from Hematoxylin using the 'Colour Deconvolution 2' plugin (Landini *et al.*, 2021). An auto-thresholded mask of cells with relatively high expression of RIPK3 was created. This mask, together with the comparatively small and non-circular shape of Kupffer cells, was used to segment individual Kupffer cells. The total RIPK3 signal within each Kupffer cell was then measured and expressed per unit area. N=90 Kupffer cells per mouse were measured.

Quantitation of apoptosis in splenic white pulp via immunohistochemistry

Sections were subjected to automated immunohistochemistry for cleaved Caspase-3 (see File **EV1**). Cleaved Caspase-3 signals were detected with a brown DAB product and sections counterstained with hematoxylin. Representative full-resolution 8-bit RGB micrographs (taken with the 60x objective; Olympus VS200) were imported into Image J 1.53t (Schindelin *et al.*, 2012) and percent area with cleaved Caspase-3 signal was analysed using a custom fully-automated macro. In brief, the cleaved Caspase-3 signal was unmixed from Hematoxylin using the 'Colour Deconvolution 2' plugin (Landini *et al.*, 2021). A predefined threshold (50-255 units) was applied, and its area expressed as a percentage of the total white pulp area. N=20 white pulp lobules per mouse were measured.

Systemic Inflammatory Response Syndrome (SIRS)

For experiments in Fig. **3A-J**, co-housed 8-week-old female C57BL/6J wildtype mice were administered either 300 µg/kg TNF (R&D Systems Cat#410-MT/CF Lot CS152103) in endotoxin-free DPBS or endotoxin-free DPBS alone (Merck Cat# TMS-012-A) via bolus tail vein injection. Core body temperature was measured hourly with a rectal probe. Mice were euthanised via carbon dioxide inhalation 9 hours after injection.

For experiments in Fig. **3K-L**, co-housed 6-month-old female C57BL/6J wildtype mice were administered either: 1) 6mg/kg of Necrostatin1s (Cell Signaling Technologies Cat#17802) in dimethyl sulfoxide via intraperitoneal injection then 15-30 minutes later given 150 µg/kg TNF (BioTimes Inc. Cat#CF09-1MG), or 150 µg/kg TNF (R&D Systems Cat#410-MT/CF Lot CS152103) in DPBS, or DPBS alone via bolus tail vein injection. Core body temperature was measured hourly with a rectal probe. Mice were euthanised via carbon dioxide inhalation 8 hours after injection or if their temperature dropped below 30ºC.

Enzyme-linked ImmunoSorbent Assay (ELISA) for mouse RIPK3

96-well ELISA plates (Sigma-Aldrich, Cat#CLS3795) were coated with rat anti-RIPK3 (clone IH12; 5μg/ml diluted in PBS) and incubated overnight at room temperature in humid conditions. Plates were then washed in PBS + 0.005% v/v Tween-20, then PBS, then distilled water. Mouse serum samples were diluted and titrated on the plate in block solution (PBS containing 1% v/v FCS, 0.002% v/v Tween-20 and 0.6% w/v skim milk powder). Plates were incubated at room temperature in humid conditions overnight. Plates were washed as before. Detection antibody, biotin-conjugated rat anti-RIPK3 (clone 8G7; 5μg/ml diluted in block solution) was added to each well. Plates were incubated for 4 hours at room temperature in humid conditions. Plates were washed as before. Streptavidin-HRP (SouthernBiotech, Cat#7100-05) was diluted in block solution and added to each well. Plates were incubated for 1 hour at room temperature in humid conditions. Plates were washed as before, and ABTS substrate solution (water containing 0.54mg/mL w/v 2'2-Azinobis (3-ethylbenzthiazoline Sulfonic Acid) diammonium salt (Sigma-Aldrich, Cat#A-1888), and 0.1M Citric Acid and 0.03% v/v Hydrogen Peroxide (H_2O_2)) was added to each well. Plates were left to develop for 30-45 minutes at room temperature protected from light. Color development was analysed on VersaMax ELISA microplate reader (Molecular Devices) using wavelengths λ=415nm minus λ=492nm.

***Tabula muris* analysis**

Robject files of the FACS-based T*abula Muris* (Tabula Muris *et al.*, 2018) dataset were downloaded from Figshare. Expression values were normalised and analysed using Seurat v4.3.0 (Butler *et al*, 2018; Hao *et al*, 2021; Satija *et al*, 2015; Stuart *et al*, 2019). Within each cell ontology and tissue origin, the percentage of cells with expression values

>0 for *Mlkl, Ripk3, Ripk1, Casp8, Mki67 and Top2a* was tabulated and colorised using Excel v16.74 (Microsoft).

Spatial transcriptomics of mouse spleen

To boost germinal centre numbers and size, one adult C57BL/6J mouse was infected intravenously with $1x10^5$ *Plasmodium berghei* parasitised red blood cells, and then drug-cured at the onset of disease symptoms as described in (Ly *et al*, 2019). Twelve days later the mouse was euthanised, spleen dissected, fixed in 10% v/v Neutral Buffered Formalin and paraffin embedded (as above). Sections of formalin-fixed paraffin-embedded spleen were cut onto slides, then spatial enhanced resolution omics-sequencing (stereo-seq) data was generated using pre-release chemistry and MGI sequencers as in (Chen *et al*, 2022a) by BGI, China. The spot-to-spot distance is 500nm and the data is binned to 50x50 spots ($25\mu m^2$). Binning was performed in stereopy (https://github.com/BGIResearch/stereopy) before being converted to an anndata file (https://github.com/scverse/anndata). The stereo-seq data was first loaded and pre-processed using the standard Scanpy workflow (https://github.com/scverse/scanpy) and then principal component analysis and Leiden clustering was performed at the bin (50x50) level. Leiden clusters were then plotted using Uniform Manifold Approximation and Projection (UMAP) and on spatial coordinates using the Squidpy package (https://github.com/scverse/squidpy). Scanpy's 'rank_genes_groups' method (https://scanpy-tutorials.readthedocs.io) was used to generate a matrix of gene by cluster populated by corresponding log-fold changes from 1 versus all t-tests. For each zone/cell type of interest a matrix is constructed by subsetting the full gene by cluster matrix generated from 'rank_genes_groups' to just the specific genes of interest. These matrices were reduced to a single column sum aggregated vector. From the vectors of scores for each 'zone' of the spleen (White Pulp, Red Pulp, Germinal Centres, and Marginal Zones), the top 5 scores within the 50th or 75th (depending on expected

transcriptional variance within zone) percentile of the maximum are selected and the corresponding Leiden clusters are aggregated hierarchically. After this aggregation of clusters, the 'rank_genes_groups' method is rerun to calculate a new set of gene rankings and log-fold changes for zones rather than clusters. The aggregated scores for genes of interest in each group are calculated for each zone. These scores are the log-fold changes for each gene within each zone. Scores for the *Casp8*, *Ripk1*, *Ripk3*, and *Mlkl* genes are then extracted from the matrices for each 'zone' of the spleen, and each individual cluster for side-by-side comparison in heatmaps. Software version used were Anndata (v0.7.5), Stereopy (v0.12.0), Scanpy (v1.9.2), Squidpy (v1.2.2), Numpy (v1.21.6), Pandas (v1.5.3), Matplotlib (v3.5.2), and Seaborn (v0.12).

Antibiotics administration

Co-housed littermates were split across two cages. The drinking water for one cage was supplemented with 1g/L ampicillin, 1g/L neomycin, 1g/L metronidazole, 0.5g/L enrofloxacin, 2.5g/L meropenem as in (Bader *et al.*, 2023). Antibiotic-supplemented water was replaced after 3 days. To minimise weight loss, both cages were given ad libitum access to Di-Vetelact supplement (Lillelund Pty Ltd). Mice were euthanised after 6 days of treatment.

RNA extraction, library preparation and sequencing

Immediately following dissection, a ~2mm^3 piece of tissue was placed in 0.5mL RNA*later* (Thermo Fisher Scientific Cat#4427575) then stored at -80°C. Samples were thawed, RNA*later* was removed then tissues were transferred into screw-capped tube pre-filled with 350 µl of RA1 buffer of NucleoSPin RNAXS kit (Macherey-Nagel Cat# SKU: 740902.250). Tissues were homogenised with 10 pcs of 3 mm Acid- Washed Zirconium Beads (OPS diagnostics Cat# BAWZ 3000-300-23) in a Qiagen TissueLyzer II

(30 Hz, 5 minutes). Homogenised samples were centrifuged (1 minute, 11,000 *g*) to remove tissue debris then RNA was purified using Nucleospin RNAXS column kit as per manufacturer's instructions without adding a carrier RNA. The purified RNA was quantified using Qubit™ RNA HS Assay kit (Thermo Fisher Scientific Cat#Q32852) and RNA integrity was visualised in high sensitivity RNA ScreenTape (Agilent Cat# 5067- 5579) using TapeStation 4200 (Agilent Cat# G2991BA). Ten nanograms of RNA were used for preparing indexed libraries using SMARTer Stranded Total RNA-Seq Pico-Input Mammalian kit v.3 (Takara Bio. Cat# SKU: 634487) as per manufacturer's instructions (except that fragmentation was performed for 3 minutes of fragmentation at 94 °C and 13 cycles was used for PCR2). The library concentration was quantified by Qubit™ dsDNA Assay kit (Thermo Fisher Cat#Q32851) and library size was determined using D1000 ScreenTape (Agilent Cat# 5067-5582) and visualised in TapeStation 4200. Equimolar amounts of the libraries were pooled and diluted to 750pM for 150-bp paired-end sequencing on a NextSeq2000 instrument (Illumina) using the P2 300- cycle kit v3 chemistry (Illumina Cat# 20046813) as per manufacturer's instructions. To produce the sequences, the base calling and quality scoring was performed by the Real Time Analysis (v2.4.6) software. The FASTQ file generation and de-multiplexing for the samples was performed by the bcl2fastq conversion software (v2.15.0.4).

Murine bulk RNA sequence analysis

The single-end 75 bp were demultiplexed using CASAVAv1.8.2 and Cutadapt (v1.9) was used for read trimming (Martin, 2011). The trimmed reads were subsequently mapped to the mouse genome (mm10) using HISAT2 (Kim *et al*, 2019). FeatureCounts from the Rsubread package (version 1.34.7) was used for read counting after which genes <2 counts per million reads (CPM) in at least 3 samples were excluded from downstream analysis (Liao *et al*, 2014, 2019). Count data were normalised using the trimmed mean of

M-values (TMM) method and differential gene expression analysis was performed using the limma-voom pipeline (limma version 3.40.6) (Law *et al*, 2014; Liao *et al.*, 2014; Robinson & Oshlack, 2010). Adjustment for multiple testing was performed per comparison using the false discovery rate (FDR) method (Benjamini & Hochberg, 1995). Heatmaps of logCPM were generated using pheatmap.

NP-KLH immunization and analysis

Immunisation was performed as previously described (Kong *et al*, 2022). 8–10-week-old *Ripk3*$^{+/+}$ or *Ripk3*$^{-/-}$ littermate mice received a single intraperitoneal injection of 100 µg 4-hydroxy-3-nitrophenylacetyl hapten coupled to keyhole limpet hemocyanin (NP-KLH; produced in-house) at a ratio of 21:1 with alum. Fourteen days after immunisation mice were euthanised via CO_2 inhalation and spleens harvested. To determine immune response to NP immunization, single-cell splenic suspensions were stained as described using antibodies to the following surface molecules: CD38 (clone:NIMR-5, in-house), CD19 (clone:1D3, cat #BD552854), IgM (clone:331.12, in-house), IgD (clone:11–26 C, in-house), Gr-1 (clone:RB6-8C5, in-house), CD138 (clone:281.2, cat #BD564068) and IgG1 (clone:X56, cat #BD550874). NP-binding was detected as described (Smith *et al*, 2000)

Mouse serum analyses

Blood was collected via cardiac puncture and immediately transferred to an EDTA-coated tube (Sarstedt AG Cat#20.1341). Blood was transferred into a clot activator tube (Sarstedt AG Cat#20.1344) and serum prepared as per the manufacturer's instructions.

Human research ethics

Ethical approval for intestinal tissue collection from participants undergoing endoscopy procedures through the Gastroenterology Department at the Royal Melbourne Hospital

was attained from the Human Research Ethics Committee (HREC): HREC 2021.074. This was in accordance with the National Health and Medical Research Council (NHMRC) National Statement on Ethical Conduct in Human Research (2008) and the Note for Guidance on Good Clinical Practice (CPMP/ICH-135/95). Site-specific governance was sought for each of the collaborating sites: WEHI and the University of Melbourne. Collaboration amongst all three participating institutions was officiated through the Melbourne Academic Centre for Health Research Collaboration Agreement (Non-Commercial). The human research in this study was performed in accordance with the principles expressed in the Helsinki Declaration. The human materials used in this study were obtained with informed consent from all subjects.

Human intestinal biopsy collection

Adult patients with or without IBD scheduled for endoscopic evaluation of the lower gastrointestinal tract (flexible sigmoidoscopy or colonoscopy) at the Gastroenterology Department at the Royal Melbourne Hospital were screened for study inclusion/exclusion. Patients were excluded based on the following criteria: active systemic (gastrointestinal and non-gastrointestinal) infection; active (solid-organ or haematological) malignancy or treatment with anti-tumour therapies; non-steroidal anti-inflammatory drug use in the last month; hereditary or familial polyposis syndromes; non-IBD forms of colitis including microscopic colitis, ischaemic colitis, diversion colitis, or diverticulitis. Eligible patients (see Table 1) were recruited and consented by the gastroenterologist (signed authorised Participant Information Sheet/Consent Form). For patients with IBD, intestinal biopsies were retrieved endoscopically from: 1) inflamed, 2) non-inflamed, or 3) marginal areas of inflammation. The same exclusion criteria as above were applied to patients without IBD (referred to as non-IBD control patients), with biopsies retrieved endoscopically from non-inflamed segments of the intestine. Boston Scientific Radial Jaw™ biopsy forceps and

Olympus EVIS EXERA III endoscopes were routinely utilised for intestinal biopsy collections. Collected biopsies were immediately placed in 10% v/v Neutral Buffered Formalin. A ratio of one part tissue to >10 parts formalin was used. Tissues were incubated in formalin at room temperature for 24-72 hours before paraffin-embedding.

Blinded histopathological scoring of intestinal inflammation

Hematoxylin and eosin-stained slides from formalin-fixed paraffin-embedded biopsies were blindly scored by an anatomical pathologist using the Robarts Histopathology Index (RHI), a validated tool for assessing IBD activity, using previously described methodology (Mosli *et al*, 2017).

Cell lines

HT29 cells were originally sourced from the American Type Culture Collection. The *RIPK1*$^{-/-}$, *RIPK3*$^{-/-}$, *MLKL*$^{-/-}$ and *CASP8*$^{-/-}$*CASP10*$^{-/-}$*MLKL*$^{-/-}$ HT29 cells have been previously reported (Jacobsen *et al*, 2022; Petrie *et al.*, 2018; Tanzer *et al.*, 2017) . Mouse dermal fibroblasts were generated in-house from the tails of wild-type C57BL/6J mice and immortalised by SV40 large T antigen as reported previously (Hildebrand *et al.*, 2014). The sex and precise age of these animals were not recorded, although our MDFs are routinely derived from tails from 8-week-old mice. Mouse dermal fibroblast lines were generated in accordance with protocols approved by the Walter and Eliza Hall Institute of Medical Research Animal Ethics Committee. The origin of cell lines was not further verified, although their morphologies and responses to necroptotic stimuli were consistent with their stated origins. Cell lines were monitored via polymerase chain reaction every ~6 months to confirm they were mycoplasma-free.

Cell culturing

HT29 cells and mouse dermal fibroblasts were maintained in Dulbecco's Modified Eagle Medium (DMEM; Life Technologies) with 8% v/v fetal calf serum (FCS), 2mM L-Glutamine, 50 U/mL penicillin and 50 U/mL streptomycin (G/P/S). Cells were incubated under humidified 10% CO_2 at 37°C.

Cell treatment

HT29 cells were treated in DMEM containing 1% v/v FCS and G/P/S. Mouse dermal fibroblasts were treated in DMEM containing 8% v/v FCS and G/P/S. Media for treatment was supplemented with: 100 ng/mL recombinant human TNF-α-Fc (produced in-house as in (Bossen *et al*, 2006)), 500 nM Smac mimetic/Compound A (provided by Tetralogic Pharmaceuticals as in (Vince *et al*, 2007)) 5 µM IDN-6556 (provided by Idun Pharmaceuticals). HT29 cells were treated for 7.5 hours. Mouse dermal fibroblasts were treated for 2 hours.

Cell lysate preparation

HT29 cells were homogenised in ice-cold RIPA buffer (10mM Tris-HCl pH 8.0, 1 mM EGTA, 2mM MgCl2, 0.5% v/v Triton X100, 0.1% w/v Na deoxycholate, 0.5% w/v SDS and 90mM NaCl) supplemented with 1x Protease & Phosphatase Inhibitor Cocktail (Cell Signaling Technology Cat#5872S) and 100 U/mL Benzonase (Sigma-Aldrich Cat#E1014).

Cell pellet preparation

Trypsinised cells were centrifuged at 671*g* (2000rpm) for 3 minutes at room temperature. The supernatant was discarded, cell pellets resuspended in 10% v/v Neutral Buffered Formalin, incubated for 15 minutes at room temperature, and centrifuged at 671*g* (2000rpm) for 3 minutes at room temperature. Cell pellets were resuspended in 50-70µL of HistoGel (Epredia Cat#HG-4000-012) pre-warmed to 56°C and then pipetted onto ice-cold

glass coverslips to set. Set pellets were stored in 70% (v/v) ethanol until paraffin embedding.

Human tissue lysate preparation

Two intestinal biopsies (each ~1-2mm^3) were pooled, immediately washed in ice-cold DPBS (Thermo Fisher Scientific Cat#14190144) supplemented with protease inhibitors (Merck Cat#4693132001) and phosphatase inhibitors (Merck Cat#4906837001), and then homogenised with a stainless steel ball bearing in a Qiagen TissueLyzer II (30 Hz, 1min) in 0.4mL of ice-cold RIPA buffer (10mM Tris-HCl pH 8.0, 1mM EGTA, 2mM MgCl2, 0.5% v/v Triton X100, 0.1% w/v sodium deoxycholate, 0.5% w/v SDS and 90mM NaCl) supplemented with 1x Protease & Phosphatase Inhibitor Cocktail (Cell Signaling Technology Cat#5872) and 100 U/mL Benzonase (Sigma-Aldrich Cat#E1014).

Necrosome quantitation

Necrosome detection was performed with a custom pipeline developed in Fiji (Schindelin *et al.*, 2012). Cells were segmented using CellPose (Stringer *et al*, 2021) and puncta detected using a difference-of-gaussian algorithm developed for graphics processing units (Haase *et al*, 2020). To avoid false-positives, puncta were filtered to be more than twice the signal of the average signal of the cell on which it appears. Number of cells with puncta, along with number of puncta per cell was recorded. Prior to detecting necrosomes in patient biopsies, the epithelial regions were segmented using FastPathology (v1.1.2) with a deep learning model trained on CD3-stained colon biopsy whole slide images (Pedersen *et al*, 2021; Pettersen *et al*, 2021). Briefly, the whole slide images were imported into FastPathology and the default model pipeline was executed using the attribute "patch-level 4". The binary mask was imported into QuPath (v0.4.3) using the

"importPyramidalTIFF.groovy" script provided at https://github.com/andreped/NoCodeSeg (Pedersen *et al.*, 2021).

Statistical tests

The number of independent experiments and the employed statistical test for each dataset is stipulated in the respective figure legend. Statistical tests were performed using Prism v.9.5.1 (GraphPad). Statistical analyses were only performed on datasets collated from at least three independent experiments. The number of independent replicates or mice is stipulated by ‘n’, and the number of dependent replicates for each dataset is stipulated by ‘N’ in the respective Fig. legend.

Data Availability Statement:

Customised image analysis macros used in this study are available upon request to the corresponding authors. The automated immunohistochemical staining protocols used in this study are available as File **EV1**. The RNA sequencing datasets generated during this study have been submitted to the Gene Expression Omnibus repository.

List of Expanded View (EV) Figures and Tables:

Fig. **EV1.** Optimisation pipeline for the immunohistochemical detection of the mouse necroptotic pathway.

Fig. **EV2.** Constitutive co-expression of necroptotic effectors is confined to fast-cycling cells within progenitors, immune and barrier populations.

Fig. **EV3**. Antibiotic-induced clusters of RIPK1/3 are not necrosomes.

Fig. **EV4.** RIPK3 is uniquely upregulated in splenic germinal centres.

Fig. **EV5.** Standardised quality control and optimisation of the immunohistochemical detection of human necroptotic proteins.

Fig. **EV6.** Automated immunohistochemistry to detect necroptotic signaling in mouse cells.

Fig. **EV7.** Assessing the specificity of immunostaining using wild-type, knockout and human RIPK3 knock-in mice.

Fig. **EV8.** Another instance of elevated intestinal apoptosis in a patient with ulcerative colitis.

Fig. **EV9.** Atlas of necroptotic pathway expression in human intestinal crypts.

Fig. **EV10.** Atlas of necroptotic pathway expression in a cohort of human intestinal biopsies.

Table **1.** Patient and clinical data related to Fig. **6** and **EV8-10**.

File **EV1** – Autostainer immunohistochemistry protocols used in this manuscript.

References:

Alvarez-Diaz S, Dillon CP, Lalaoui N, Tanzer MC, Rodriguez DA, Lin A, Lebois M, Hakem R, Josefsson EC, O'Reilly LA *et al* (2016) The Pseudokinase MLKL and the Kinase RIPK3 Have Distinct Roles in Autoimmune Disease Caused by Loss of Death-Receptor-Induced Apoptosis. *Immunity* 45: 513-526

Ananthakrishnan AN (2015) Epidemiology and risk factors for IBD. *Nat Rev Gastroenterol Hepatol* 12: 205-217

Bader SM, Preston SP, Saliba K, Lipszyc A, Grant ZL, Mackiewicz L, Baldi A, Hempel A, Clark MP, Peiris T *et al* (2023) Endothelial Caspase-8 prevents fatal necroptotic hemorrhage caused by commensal bacteria. *Cell Death Differ* 30: 27-36

Ben-Moshe S, Shapira Y, Moor AE, Manco R, Veg T, Bahar Halpern K, Itzkovitz S (2019) Spatial sorting enables comprehensive characterization of liver zonation. *Nat Metab* 1: 899-911

Benjamini Y, Hochberg Y (1995) Controlling the False Discovery Rate: A Practical and Powerful Approach to Multiple Testing. *Journal of the Royal Statistical Society: Series B (Methodological)* 57: 289-300

Berkova L, Fazilaty H, Yang Q, Kubovciak J, Stastna M, Hrckulak D, Vojtechova M, Dalessi T, Brugger MD, Hausmann G *et al* (2023) Terminal differentiation of villus tip enterocytes is governed by distinct Tgfbeta superfamily members. *EMBO Rep* 24: e56454

Bobrow MN, Moen PT, Jr. (2001) Tyramide signal amplification (TSA) systems for the enhancement of ISH signals in cytogenetics. *Curr Protoc Cytom* Chapter 8: Unit 8 9

Bossen C, Ingold K, Tardivel A, Bodmer JL, Gaide O, Hertig S, Ambrose C, Tschopp J, Schneider P (2006) Interactions of tumor necrosis factor (TNF) and TNF receptor family members in the mouse and human. *J Biol Chem* 281: 13964-13971

Butler A, Hoffman P, Smibert P, Papalexi E, Satija R (2018) Integrating single-cell transcriptomic data across different conditions, technologies, and species. *Nat Biotechnol* 36: 411-420

1070 Chen A, Liao S, Cheng M, Ma K, Wu L, Lai Y, Qiu X, Yang J, Xu J, Hao S *et al* (2022a) Spatiotemporal
1071 transcriptomic atlas of mouse organogenesis using DNA nanoball-patterned arrays. *Cell* 185: 1777-
1072 1792 e1721
1073 Chen W, Zhou Z, Li L, Zhong CQ, Zheng X, Wu X, Zhang Y, Ma H, Huang D, Li W *et al* (2013) Diverse
1074 sequence determinants control human and mouse receptor interacting protein 3 (RIP3) and mixed
1075 lineage kinase domain-like (MLKL) interaction in necroptotic signaling. *J Biol Chem* 288: 16247-
1076 16261
1077 Chen X, Li W, Ren J, Huang D, He WT, Song Y, Yang C, Li W, Zheng X, Chen P *et al* (2014)
1078 Translocation of mixed lineage kinase domain-like protein to plasma membrane leads to necrotic
1079 cell death. *Cell Res* 24: 105-121
1080 Chen X, Zhu R, Zhong J, Ying Y, Wang W, Cao Y, Cai H, Li X, Shuai J, Han J (2022b) Mosaic
1081 composition of RIP1-RIP3 signalling hub and its role in regulating cell death. *Nat Cell Biol*
1082 Cho YS, Challa S, Moquin D, Genga R, Ray TD, Guildford M, Chan FK (2009) Phosphorylation-driven
1083 assembly of the RIP1-RIP3 complex regulates programmed necrosis and virus-induced
1084 inflammation. *Cell* 137: 1112-1123
1085 Choi ME, Price DR, Ryter SW, Choi AMK (2019) Necroptosis: a crucial pathogenic mediator of
1086 human disease. *JCI Insight* 4
1087 Cook WD, Moujalled DM, Ralph TJ, Lock P, Young SN, Murphy JM, Vaux DL (2014) RIPK1- and RIPK3-
1088 induced cell death mode is determined by target availability. *Cell Death Differ* 21: 1600-1612
1089 Davies KA, Fitzgibbon C, Young SN, Garnish SE, Yeung W, Coursier D, Birkinshaw RW, Sandow JJ,
1090 Lehmann WIL, Liang LY *et al* (2020) Distinct pseudokinase domain conformations underlie
1091 divergent activation mechanisms among vertebrate MLKL orthologues. *Nat Commun* 11: 3060
1092 de Almagro MC, Goncharov T, Izrael-Tomasevic A, Duttler S, Kist M, Varfolomeev E, Wu X, Lee WP,
1093 Murray J, Webster JD *et al* (2017) Coordinated ubiquitination and phosphorylation of RIP1
1094 regulates necroptotic cell death. *Cell Death Differ* 24: 26-37

1095 Degterev A, Hitomi J, Germscheid M, Ch'en IL, Korkina O, Teng X, Abbott D, Cuny GD, Yuan C,
1096 Wagner G *et al* (2008) Identification of RIP1 kinase as a specific cellular target of necrostatins. *Nat*
1097 *Chem Biol* 4: 313-321
1098 Degterev A, Huang Z, Boyce M, Li Y, Jagtap P, Mizushima N, Cuny GD, Mitchison TJ, Moskowitz MA,
1099 Yuan J (2005) Chemical inhibitor of nonapoptotic cell death with therapeutic potential for ischemic
1100 brain injury. *Nat Chem Biol* 1: 112-119
1101 Devos M, Tanghe G, Gilbert B, Dierick E, Verheirstraeten M, Nemegeer J, de Reuver R, Lefebvre S,
1102 De Munck J, Rehwinkel J *et al* (2020) Sensing of endogenous nucleic acids by ZBP1 induces
1103 keratinocyte necroptosis and skin inflammation. *J Exp Med* 217
1104 Doerflinger M, Deng Y, Whitney P, Salvamoser R, Engel S, Kueh AJ, Tai L, Bachem A, Gressier E,
1105 Geoghegan ND *et al* (2020) Flexible Usage and Interconnectivity of Diverse Cell Death Pathways
1106 Protect against Intracellular Infection. *Immunity* 53: 533-547 e537
1107 Dominguez S, Varfolomeev E, Brendza R, Stark K, Tea J, Imperio J, Ngu H, Earr T, Foreman O,
1108 Webster JD *et al* (2021) Genetic inactivation of RIP1 kinase does not ameliorate disease in a mouse
1109 model of ALS. *Cell Death Differ* 28: 915-931
1110 Duprez L, Takahashi N, Van Hauwermeiren F, Vandendriessche B, Goossens V, Vanden Berghe T,
1111 Declercq W, Libert C, Cauwels A, Vandenabeele P (2011) RIP kinase-dependent necrosis drives
1112 lethal systemic inflammatory response syndrome. *Immunity* 35: 908-918
1113 Fang Z, Wei H, Gou W, Chen L, Bi C, Hou W, Li Y (2021) Recent progress in small-molecule inhibitors
1114 for critical therapeutic targets of necroptosis. *Future Med Chem* 13: 817-837
1115 Fletcher-Etherington A, Nobre L, Nightingale K, Antrobus R, Nichols J, Davison AJ, Stanton RJ,
1116 Weekes MP (2020) Human cytomegalovirus protein pUL36: A dual cell death pathway inhibitor.
1117 *Proc Natl Acad Sci U S A* 117: 18771-18779

1118 Garnish SE, Martin KR, Kauppi M, Jackson VE, Ambrose R, Eng VV, Chiou S, Meng Y, Frank D, Tovey
1119 Crutchfield EC *et al* (2023) A common human MLKL polymorphism confers resistance to negative
1120 regulation by phosphorylation. *Nat Commun* 14: 6046
1121 Garnish SE, Meng Y, Koide A, Sandow JJ, Denbaum E, Jacobsen AV, Yeung W, Samson AL, Horne CR,
1122 Fitzgibbon C *et al* (2021) Conformational interconversion of MLKL and disengagement from RIPK3
1123 precede cell death by necroptosis. *Nat Commun* 12: 2211
1124 Ge Y, Ezzell RM, Warren HS (2000) Localization of endotoxin in the rat intestinal epithelium. *J Infect*
1125 *Dis* 182: 873-881
1126 Geiger T, Velic A, Macek B, Lundberg E, Kampf C, Nagaraj N, Uhlen M, Cox J, Mann M (2013) Initial
1127 quantitative proteomic map of 28 mouse tissues using the SILAC mouse. *Mol Cell Proteomics* 12:
1128 1709-1722
1129 Gevers D, Kugathasan S, Denson LA, Vazquez-Baeza Y, Van Treuren W, Ren B, Schwager E, Knights D,
1130 Song SJ, Yassour M *et al* (2014) The treatment-naive microbiome in new-onset Crohn's disease. *Cell*
1131 *Host Microbe* 15: 382-392
1132 Graham DB, Xavier RJ (2020) Pathway paradigms revealed from the genetics of inflammatory
1133 bowel disease. *Nature* 578: 527-539
1134 Gunther C, Buchen B, He GW, Hornef M, Torow N, Neumann H, Wittkopf N, Martini E, Basic M,
1135 Bleich A *et al* (2015) Caspase-8 controls the gut response to microbial challenges by Tnf-alpha-
1136 dependent and independent pathways. *Gut* 64: 601-610
1137 Gunther C, Martini E, Wittkopf N, Amann K, Weigmann B, Neumann H, Waldner MJ, Hedrick SM,
1138 Tenzer S, Neurath MF *et al* (2011) Caspase-8 regulates TNF-alpha-induced epithelial necroptosis
1139 and terminal ileitis. *Nature* 477: 335-339
1140 Gupta K, Liu B (2021) PLK1-mediated S369 phosphorylation of RIPK3 during G2 and M phases
1141 enables its ripoptosome incorporation and activity. *iScience* 24: 102320

1142 Haase R, Royer LA, Steinbach P, Schmidt D, Dibrov A, Schmidt U, Weigert M, Maghelli N, Tomancak
1143 P, Jug F *et al* (2020) CLIJ: GPU-accelerated image processing for everyone. *Nat Methods* 17: 5-6
1144 Haber AL, Biton M, Rogel N, Herbst RH, Shekhar K, Smillie C, Burgin G, Delorey TM, Howitt MR,
1145 Katz Y *et al* (2017) A single-cell survey of the small intestinal epithelium. *Nature* 551: 333-339
1146 Hao Y, Hao S, Andersen-Nissen E, Mauck WM, 3rd, Zheng S, Butler A, Lee MJ, Wilk AJ, Darby C,
1147 Zager M *et al* (2021) Integrated analysis of multimodal single-cell data. *Cell* 184: 3573-3587 e3529
1148 Harris PA, Berger SB, Jeong JU, Nagilla R, Bandyopadhyay D, Campobasso N, Capriotti CA, Cox JA,
1149 Dare L, Dong X *et al* (2017) Discovery of a First-in-Class Receptor Interacting Protein 1 (RIP1) Kinase
1150 Specific Clinical Candidate (GSK2982772) for the Treatment of Inflammatory Diseases. *J Med Chem*
1151 60: 1247-1261
1152 He P, Ai T, Yang ZH, Wu J, Han J (2021) Detection of necroptosis by phospho-MLKL
1153 immunohistochemical labeling. *STAR Protoc* 2: 100251
1154 He S, Liang Y, Shao F, Wang X (2011) Toll-like receptors activate programmed necrosis in
1155 macrophages through a receptor-interacting kinase-3-mediated pathway. *Proc Natl Acad Sci U S A*
1156 108: 20054-20059
1157 He S, Wang L, Miao L, Wang T, Du F, Zhao L, Wang X (2009) Receptor interacting protein kinase-3
1158 determines cellular necrotic response to TNF-alpha. *Cell* 137: 1100-1111
1159 Hildebrand JM, Kauppi M, Majewski IJ, Liu Z, Cox AJ, Miyake S, Petrie EJ, Silk MA, Li Z, Tanzer MC *et*
1160 *al* (2020) A missense mutation in the MLKL brace region promotes lethal neonatal inflammation
1161 and hematopoietic dysfunction. *Nat Commun* 11: 3150
1162 Hildebrand JM, Tanzer MC, Lucet IS, Young SN, Spall SK, Sharma P, Pierotti C, Garnier JM, Dobson
1163 RC, Webb AI *et al* (2014) Activation of the pseudokinase MLKL unleashes the four-helix bundle
1164 domain to induce membrane localization and necroptotic cell death. *Proc Natl Acad Sci U S A* 111:
1165 15072-15077

1166 Horne CR, Samson AL, Murphy JM (2023) The web of death: the expanding complexity of
1167 necroptotic signaling. *Trends Cell Biol* 33: 162-174
1168 Ito Y, Ofengeim D, Najafov A, Das S, Saberi S, Li Y, Hitomi J, Zhu H, Chen H, Mayo L *et al* (2016)
1169 RIPK1 mediates axonal degeneration by promoting inflammation and necroptosis in ALS. *Science*
1170 353: 603-608
1171 Jacobsen AV, Pierotti CL, Lowes KN, Au AE, Zhang Y, Etemadi N, Fitzgibbon C, Kersten WJA, Samson
1172 AL, van Delft MF *et al* (2022) The Lck inhibitor, AMG-47a, blocks necroptosis and implicates RIPK1
1173 in signalling downstream of MLKL. *Cell Death Dis* 13: 291
1174 Kaiser WJ, Sridharan H, Huang C, Mandal P, Upton JW, Gough PJ, Sehon CA, Marquis RW, Bertin J,
1175 Mocarski ES (2013) Toll-like receptor 3-mediated necrosis via TRIF, RIP3, and MLKL. *J Biol Chem*
1176 288: 31268-31279
1177 Kaiser WJ, Upton JW, Long AB, Livingston-Rosanoff D, Daley-Bauer LP, Hakem R, Caspary T,
1178 Mocarski ES (2011) RIP3 mediates the embryonic lethality of caspase-8-deficient mice. *Nature* 471:
1179 368-372
1180 Kelliher MA, Grimm S, Ishida Y, Kuo F, Stanger BZ, Leder P (1998) The death domain kinase RIP
1181 mediates the TNF-induced NF-kappaB signal. *Immunity* 8: 297-303
1182 Kim D, Paggi JM, Park C, Bennett C, Salzberg SL (2019) Graph-based genome alignment and
1183 genotyping with HISAT2 and HISAT-genotype. *Nat Biotechnol* 37: 907-915
1184 Kobayashi T, Siegmund B, Le Berre C, Wei SC, Ferrante M, Shen B, Bernstein CN, Danese S, Peyrin-
1185 Biroulet L, Hibi T (2020) Ulcerative colitis. *Nat Rev Dis Primers* 6: 74
1186 Kong IY, Trezise S, Light A, Todorovski I, Arnau GM, Gadipally S, Yoannidis D, Simpson KJ, Dong X,
1187 Whitehead L *et al* (2022) Epigenetic modulators of B cell fate identified through coupled
1188 phenotype-transcriptome analysis. *Cell Death Differ* 29: 2519-2530
1189 Landini G, Martinelli G, Piccinini F (2021) Colour deconvolution: stain unmixing in histological
1190 imaging. *Bioinformatics* 37: 1485-1487

1191 Law CW, Chen Y, Shi W, Smyth GK (2014) voom: Precision weights unlock linear model analysis
1192 tools for RNA-seq read counts. *Genome Biol* 15: R29
1193 Li D, Meng L, Xu T, Su Y, Liu X, Zhang Z, Wang X (2017) RIPK1-RIPK3-MLKL-dependent necrosis
1194 promotes the aging of mouse male reproductive system. *Elife* 6
1195 Li L, Huang K, Ruan C, Han J, Zhang Y (2022) Immunostaining of phospho-RIPK3 in L929 cells,
1196 murine yolk sacs, ceca, and small intestines. *STAR Protoc* 3: 101517
1197 Li X, Zhang M, Huang X, Liang W, Li G, Lu X, Li Y, Pan H, Shi L, Zhu H *et al* (2020) Ubiquitination of
1198 RIPK1 regulates its activation mediated by TNFR1 and TLRs signaling in distinct manners. *Nat*
1199 *Commun* 11: 6364
1200 Li X, Zhong CQ, Wu R, Xu X, Yang ZH, Cai S, Wu X, Chen X, Yin Z, He Q *et al* (2021) RIP1-dependent
1201 linear and nonlinear recruitments of caspase-8 and RIP3 respectively to necrosome specify distinct
1202 cell death outcomes. *Protein Cell* 12: 858-876
1203 Liao Y, Smyth GK, Shi W (2014) featureCounts: an efficient general purpose program for assigning
1204 sequence reads to genomic features. *Bioinformatics* 30: 923-930
1205 Liao Y, Smyth GK, Shi W (2019) The R package Rsubread is easier, faster, cheaper and better for
1206 alignment and quantification of RNA sequencing reads. *Nucleic Acids Res* 47: e47
1207 Liccardi G, Ramos Garcia L, Tenev T, Annibaldi A, Legrand AJ, Robertson D, Feltham R, Anderton H,
1208 Darding M, Peltzer N *et al* (2019) RIPK1 and Caspase-8 Ensure Chromosome Stability
1209 Independently of Their Role in Cell Death and Inflammation. *Mol Cell* 73: 413-428 e417
1210 Linkermann A, Brasen JH, Darding M, Jin MK, Sanz AB, Heller JO, De Zen F, Weinlich R, Ortiz A,
1211 Walczak H *et al* (2013) Two independent pathways of regulated necrosis mediate ischemia-
1212 reperfusion injury. *Proc Natl Acad Sci U S A* 110: 12024-12029
1213 Liu Z, Nailwal H, Rector J, Rahman MM, Sam R, McFadden G, Chan FK (2021) A class of viral inducer
1214 of degradation of the necroptosis adaptor RIPK3 regulates virus-induced inflammation. *Immunity*
1215 54: 247-258 e247

1216 Lu Z, Van Eeckhoutte HP, Liu G, Nair PM, Jones B, Gillis CM, Nalkurthi BC, Verhamme F, Buyle-
1217 Huybrecht T, Vandenabeele P *et al* (2021) Necroptosis Signaling Promotes Inflammation, Airway
1218 Remodeling, and Emphysema in Chronic Obstructive Pulmonary Disease. *Am J Respir Crit Care Med*
1219 204: 667-681

1220 Luedde M, Lutz M, Carter N, Sosna J, Jacoby C, Vucur M, Gautheron J, Roderburg C, Borg N,
1221 Reisinger F *et al* (2014) RIP3, a kinase promoting necroptotic cell death, mediates adverse
1222 remodelling after myocardial infarction. *Cardiovasc Res* 103: 206-216

1223 Ly A, Liao Y, Pietrzak H, Ioannidis LJ, Sidwell T, Gloury R, Doerflinger M, Triglia T, Qin RZ, Groom JR
1224 *et al* (2019) Transcription Factor T-bet in B Cells Modulates Germinal Center Polarization and
1225 Antibody Affinity Maturation in Response to Malaria. *Cell Rep* 29: 2257-2269 e2256

1226 Martin M (2011) Cutadapt removes adapter sequences from high-throughput sequencing reads.
1227 *2011* 17: 3

1228 Matsuzawa-Ishimoto Y, Shono Y, Gomez LE, Hubbard-Lucey VM, Cammer M, Neil J, Dewan MZ,
1229 Lieberman SR, Lazrak A, Marinis JM *et al* (2017) Autophagy protein ATG16L1 prevents necroptosis
1230 in the intestinal epithelium. *J Exp Med* 214: 3687-3705

1231 Moor AE, Harnik Y, Ben-Moshe S, Massasa EE, Rozenberg M, Eilam R, Bahar Halpern K, Itzkovitz S
1232 (2018) Spatial Reconstruction of Single Enterocytes Uncovers Broad Zonation along the Intestinal
1233 Villus Axis. *Cell* 175: 1156-1167 e1115

1234 Mosli MH, Feagan BG, Zou G, Sandborn WJ, D'Haens G, Khanna R, Shackelton LM, Walker CW,
1235 Nelson S, Vandervoort MK *et al* (2017) Development and validation of a histological index for UC.
1236 *Gut* 66: 50-58

1237 Murphy JM, Czabotar PE, Hildebrand JM, Lucet IS, Zhang JG, Alvarez-Diaz S, Lewis R, Lalaoui N,
1238 Metcalf D, Webb AI *et al* (2013) The pseudokinase MLKL mediates necroptosis via a molecular
1239 switch mechanism. *Immunity* 39: 443-453

1240 Naito MG, Xu D, Amin P, Lee J, Wang H, Li W, Kelliher M, Pasparakis M, Yuan J (2020) Sequential
1241 activation of necroptosis and apoptosis cooperates to mediate vascular and neural pathology in
1242 stroke. *Proc Natl Acad Sci U S A* 117: 4959-4970
1243 Najafov A, Zervantonakis IK, Mookhtiar AK, Greninger P, March RJ, Egan RK, Luu HS, Stover DG,
1244 Matulonis UA, Benes CH *et al* (2018) BRAF and AXL oncogenes drive RIPK3 expression loss in
1245 cancer. *PLoS Biol* 16: e2005756
1246 Negroni A, Colantoni E, Pierdomenico M, Palone F, Costanzo M, Oliva S, Tiberti A, Cucchiara S,
1247 Stronati L (2017) RIP3 AND pMLKL promote necroptosis-induced inflammation and alter
1248 membrane permeability in intestinal epithelial cells. *Dig Liver Dis* 49: 1201-1210
1249 Newton K, Dugger DL, Maltzman A, Greve JM, Hedehus M, Martin-McNulty B, Carano RA, Cao TC,
1250 van Bruggen N, Bernstein L *et al* (2016) RIPK3 deficiency or catalytically inactive RIPK1 provides
1251 greater benefit than MLKL deficiency in mouse models of inflammation and tissue injury. *Cell*
1252 *Death Differ* 23: 1565-1576
1253 Newton K, Dugger DL, Wickliffe KE, Kapoor N, de Almagro MC, Vucic D, Komuves L, Ferrando RE,
1254 French DM, Webster J *et al* (2014) Activity of protein kinase RIPK3 determines whether cells die by
1255 necroptosis or apoptosis. *Science* 343: 1357-1360
1256 Newton K, Sun X, Dixit VM (2004) Kinase RIP3 is dispensable for normal NF-kappa Bs, signaling by
1257 the B-cell and T-cell receptors, tumor necrosis factor receptor 1, and Toll-like receptors 2 and 4.
1258 *Mol Cell Biol* 24: 1464-1469
1259 O'Reilly LA, Divisekera U, Newton K, Scalzo K, Kataoka T, Puthalakath H, Ito M, Huang DC, Strasser A
1260 (2004) Modifications and intracellular trafficking of FADD/MORT1 and caspase-8 after stimulation
1261 of T lymphocytes. *Cell Death Differ* 11: 724-736
1262 Palmer SN, Chappidi S, Pinkham C, Hancks DC (2021) Evolutionary Profile for (Host and Viral) MLKL
1263 Indicates Its Activities as a Battlefront for Extensive Counteradaptation. *Mol Biol Evol* 38: 5405-
1264 5422

1265 Park JH, Kotani T, Konno T, Setiawan J, Kitamura Y, Imada S, Usui Y, Hatano N, Shinohara M, Saito Y
1266 *et al* (2016) Promotion of Intestinal Epithelial Cell Turnover by Commensal Bacteria: Role of Short-
1267 Chain Fatty Acids. *PLoS One* 11: e0156334
1268 Pearson JS, Giogha C, Muhlen S, Nachbur U, Pham CL, Zhang Y, Hildebrand JM, Oates CV, Lung TW,
1269 Ingle D *et al* (2017) EspL is a bacterial cysteine protease effector that cleaves RHIM proteins to
1270 block necroptosis and inflammation. *Nat Microbiol* 2: 16258
1271 Pedersen A, Valla A, Bofin M, De Frutos JP, Reinersten I, Smistad E (2021) FastPathology: An Open-
1272 Source Platform for Deep Learning-Based Research and Decision Support in Digital Pathology. *IEEE*
1273 *Access* 9: 58216-58229
1274 Percie du Sert N, Hurst V, Ahluwalia A, Alam S, Avey MT, Baker M, Browne WJ, Clark A, Cuthill IC,
1275 Dirnagl U *et al* (2020) The ARRIVE guidelines 2.0: Updated guidelines for reporting animal research.
1276 *PLoS Biol* 18: e3000410
1277 Petrie EJ, Sandow JJ, Jacobsen AV, Smith BJ, Griffin MDW, Lucet IS, Dai W, Young SN, Tanzer MC,
1278 Wardak A *et al* (2018) Conformational switching of the pseudokinase domain promotes human
1279 MLKL tetramerization and cell death by necroptosis. *Nat Commun* 9: 2422
1280 Petrie EJ, Sandow JJ, Lehmann WIL, Liang LY, Coursier D, Young SN, Kersten WJA, Fitzgibbon C,
1281 Samson AL, Jacobsen AV *et al* (2019) Viral MLKL Homologs Subvert Necroptotic Cell Death by
1282 Sequestering Cellular RIPK3. *Cell Rep* 28: 3309-3319 e3305
1283 Pettersen HS, Belevich I, Royset ES, Smistad E, Simpson MR, Jokitalo E, Reinertsen I, Bakke I,
1284 Pedersen A (2021) Code-Free Development and Deployment of Deep Segmentation Models for
1285 Digital Pathology. *Front Med (Lausanne)* 8: 816281
1286 Pierdomenico M, Negroni A, Stronati L, Vitali R, Prete E, Bertin J, Gough PJ, Aloi M, Cucchiara S
1287 (2014) Necroptosis is active in children with inflammatory bowel disease and contributes to
1288 heighten intestinal inflammation. *Am J Gastroenterol* 109: 279-287

1289 Preston SP, Stutz MD, Allison CC, Nachbur U, Gouil Q, Tran BM, Duvivier V, Arandjelovic P, Cooney
1290 JP, Mackiewicz L *et al* (2022) Epigenetic Silencing of RIPK3 in Hepatocytes Prevents MLKL-mediated
1291 Necroptosis From Contributing to Liver Pathologies. *Gastroenterology* 163: 1643-1657 e1614
1292 Ramirez MLG, Salvesen GS (2018) A primer on caspase mechanisms. *Semin Cell Dev Biol* 82: 79-85
1293 Rickard JA, O'Donnell JA, Evans JM, Lalaoui N, Poh AR, Rogers T, Vince JE, Lawlor KE, Ninnis RL,
1294 Anderton H *et al* (2014) RIPK1 regulates RIPK3-MLKL-driven systemic inflammation and emergency
1295 hematopoiesis. *Cell* 157: 1175-1188
1296 Robinson MD, Oshlack A (2010) A scaling normalization method for differential expression analysis
1297 of RNA-seq data. *Genome Biol* 11: R25
1298 Roda G, Chien Ng S, Kotze PG, Argollo M, Panaccione R, Spinelli A, Kaser A, Peyrin-Biroulet L,
1299 Danese S (2020) Crohn's disease. *Nat Rev Dis Primers* 6: 22
1300 Rodriguez DA, Quarato G, Liedmann S, Tummers B, Zhang T, Guy C, Crawford JC, Palacios G,
1301 Pelletier S, Kalkavan H *et al* (2022) Caspase-8 and FADD prevent spontaneous ZBP1 expression and
1302 necroptosis. *Proc Natl Acad Sci U S A* 119: e2207240119
1303 Rodriguez DA, Weinlich R, Brown S, Guy C, Fitzgerald P, Dillon CP, Oberst A, Quarato G, Low J,
1304 Cripps JG *et al* (2016) Characterization of RIPK3-mediated phosphorylation of the activation loop of
1305 MLKL during necroptosis. *Cell Death Differ* 23: 76-88
1306 Salmena L, Lemmers B, Hakem A, Matysiak-Zablocki E, Murakami K, Au PY, Berry DM, Tamblyn L,
1307 Shehabeldin A, Migon E *et al* (2003) Essential role for caspase 8 in T-cell homeostasis and T-cell-
1308 mediated immunity. *Genes Dev* 17: 883-895
1309 Samson AL, Fitzgibbon C, Patel KM, Hildebrand JM, Whitehead LW, Rimes JS, Jacobsen AV, Horne
1310 CR, Gavin XJ, Young SN *et al* (2021a) A toolbox for imaging RIPK1, RIPK3, and MLKL in mouse and
1311 human cells. *Cell Death Differ* 28: 2126-2144
1312 Samson AL, Garnish SE, Hildebrand JM, Murphy JM (2021b) Location, location, location: A
1313 compartmentalized view of TNF-induced necroptotic signaling. *Sci Signal* 14

1314 Samson AL, Zhang Y, Geoghegan ND, Gavin XJ, Davies KA, Mlodzianoski MJ, Whitehead LW, Frank D,
1315 Garnish SE, Fitzgibbon C *et al* (2020) MLKL trafficking and accumulation at the plasma membrane
1316 control the kinetics and threshold for necroptosis. *Nat Commun* 11: 3151
1317 Satija R, Farrell JA, Gennert D, Schier AF, Regev A (2015) Spatial reconstruction of single-cell gene
1318 expression data. *Nat Biotechnol* 33: 495-502
1319 Schindelin J, Arganda-Carreras I, Frise E, Kaynig V, Longair M, Pietzsch T, Preibisch S, Rueden C,
1320 Saalfeld S, Schmid B *et al* (2012) Fiji: an open-source platform for biological-image analysis. *Nat*
1321 *Methods* 9: 676-682
1322 Schwarzer R, Jiao H, Wachsmuth L, Tresch A, Pasparakis M (2020) FADD and Caspase-8 Regulate
1323 Gut Homeostasis and Inflammation by Controlling MLKL- and GSDMD-Mediated Death of Intestinal
1324 Epithelial Cells. *Immunity* 52: 978-993 e976
1325 Shi Y, Cui X, Sun Y, Zhao Q, Liu T (2020) Intestinal vitamin D receptor signaling ameliorates dextran
1326 sulfate sodium-induced colitis by suppressing necroptosis of intestinal epithelial cells. *FASEB J* 34:
1327 13494-13506
1328 Smith KG, Light A, O'Reilly LA, Ang SM, Strasser A, Tarlinton D (2000) bcl-2 transgene expression
1329 inhibits apoptosis in the germinal center and reveals differences in the selection of memory B cells
1330 and bone marrow antibody-forming cells. *J Exp Med* 191: 475-484
1331 Stringer C, Wang T, Michaelos M, Pachitariu M (2021) Cellpose: a generalist algorithm for cellular
1332 segmentation. *Nat Methods* 18: 100-106
1333 Stuart T, Butler A, Hoffman P, Hafemeister C, Papalexi E, Mauck WM, 3rd, Hao Y, Stoeckius M,
1334 Smibert P, Satija R (2019) Comprehensive Integration of Single-Cell Data. *Cell* 177: 1888-1902
1335 e1821
1336 Sun L, Wang H, Wang Z, He S, Chen S, Liao D, Wang L, Yan J, Liu W, Lei X *et al* (2012) Mixed lineage
1337 kinase domain-like protein mediates necrosis signaling downstream of RIP3 kinase. *Cell* 148: 213-
1338 227

1339 Tabula Muris C, Overall c, Logistical c, Organ c, processing, Library p, sequencing, Computational
1340 data a, Cell type a, Writing g *et al* (2018) Single-cell transcriptomics of 20 mouse organs creates a
1341 Tabula Muris. *Nature* 562: 367-372
1342 Tanzer MC, Khan N, Rickard JA, Etemadi N, Lalaoui N, Spall SK, Hildebrand JM, Segal D, Miasari M,
1343 Chau D *et al* (2017) Combination of IAP antagonist and IFNgamma activates novel caspase-10- and
1344 RIPK1-dependent cell death pathways. *Cell Death Differ* 24: 481-491
1345 Tanzer MC, Matti I, Hildebrand JM, Young SN, Wardak A, Tripaydonis A, Petrie EJ, Mildenhall AL,
1346 Vaux DL, Vince JE *et al* (2016) Evolutionary divergence of the necroptosis effector MLKL. *Cell Death*
1347 *Differ* 23: 1185-1197
1348 Tisch N, Mogler C, Stojanovic A, Luck R, Korhonen EA, Ellerkmann A, Adler H, Singhal M,
1349 Schermann G, Erkert L *et al* (2022) Caspase-8 in endothelial cells maintains gut homeostasis and
1350 prevents small bowel inflammation in mice. *EMBO Mol Med*: e14121
1351 Tovey Crutchfield EC, Garnish SE, Day J, Anderton H, Chiou S, Hempel A, Hall C, Patel KM,
1352 Gangatirkar P, Martin KR *et al* (2023) MLKL deficiency protects against low-grade, sterile
1353 inflammation in aged mice. *Cell Death Differ* 30: 1059-1071
1354 Uhlen M, Fagerberg L, Hallstrom BM, Lindskog C, Oksvold P, Mardinoglu A, Sivertsson A, Kampf C,
1355 Sjostedt E, Asplund A *et al* (2015) Proteomics. Tissue-based map of the human proteome. *Science*
1356 347: 1260419
1357 Upton JW, Kaiser WJ, Mocarski ES (2010) Virus inhibition of RIP3-dependent necrosis. *Cell Host*
1358 *Microbe* 7: 302-313
1359 Vince JE, Wong WW, Khan N, Feltham R, Chau D, Ahmed AU, Benetatos CA, Chunduru SK, Condon
1360 SM, McKinlay M *et al* (2007) IAP antagonists target cIAP1 to induce TNFalpha-dependent
1361 apoptosis. *Cell* 131: 682-693
1362 Vlantis K, Wullaert A, Polykratis A, Kondylis V, Dannappel M, Schwarzer R, Welz P, Corona T,
1363 Walczak H, Weih F *et al* (2016) NEMO Prevents RIP Kinase 1-Mediated Epithelial Cell Death and

1364 Chronic Intestinal Inflammation by NF-kappaB-Dependent and -Independent Functions. *Immunity*
1365 44: 553-567
1366 Vucur M, Ghallab A, Schneider AT, Adili A, Cheng M, Castoldi M, Singer MT, Buttner V, Keysberg LS,
1367 Kusgens L *et al* (2023) Sublethal necroptosis signaling promotes inflammation and liver cancer.
1368 *Immunity* 56: 1578-1595 e1578
1369 Wang H, Sun L, Su L, Rizo J, Liu L, Wang LF, Wang FS, Wang X (2014) Mixed lineage kinase domain-
1370 like protein MLKL causes necrotic membrane disruption upon phosphorylation by RIP3. *Mol Cell*
1371 54: 133-146
1372 Wang R, Li H, Wu J, Cai ZY, Li B, Ni H, Qiu X, Chen H, Liu W, Yang ZH *et al* (2020a) Gut stem cell
1373 necroptosis by genome instability triggers bowel inflammation. *Nature* 580: 386-390
1374 Wang T, Perera ND, Chiam MDF, Cuic B, Wanniarachchillage N, Tomas D, Samson AL, Cawthorne W,
1375 Valor EN, Murphy JM *et al* (2020b) Necroptosis is dispensable for motor neuron degeneration in a
1376 mouse model of ALS. *Cell Death Differ* 27: 1728-1739
1377 Webster JD, Solon M, Haller S, Newton K (2018) Detection of Necroptosis by Phospho-RIPK3
1378 Immunohistochemical Labeling. *Methods Mol Biol* 1857: 153-160
1379 Weisel K, Scott N, Berger S, Wang S, Brown K, Powell M, Broer M, Watts C, Tompson DJ, Burriss SW
1380 *et al* (2021) A randomised, placebo-controlled study of RIPK1 inhibitor GSK2982772 in patients
1381 with active ulcerative colitis. *BMJ Open Gastroenterol* 8
1382 Xie Y, Zhao Y, Shi L, Li W, Chen K, Li M, Chen X, Zhang H, Li T, Matsuzawa-Ishimoto Y *et al* (2020) Gut
1383 epithelial TSC1/mTOR controls RIPK3-dependent necroptosis in intestinal inflammation and cancer.
1384 *J Clin Invest* 130: 2111-2128
1385 Xu J, Li S, Jin W, Zhou H, Zhong T, Cheng X, Fu Y, Xiao P, Cheng H, Wang D *et al* (2023) Epithelial
1386 Gab1 calibrates RIPK3-dependent necroptosis to prevent intestinal inflammation. *JCI Insight* 8
1387 Yeap HW, Chen KW (2022) RIPK1 and RIPK3 in antibacterial defence. *Biochem Soc Trans* 50: 1583-
1388 1594

1389 Zelic M, Kelliher MA (2018) Analyzing Necroptosis Using an RIPK1 Kinase Inactive Mouse Model of
1390 TNF Shock. *Methods Mol Biol* 1857: 125-134

1391 Zelic M, Roderick JE, O'Donnell JA, Lehman J, Lim SE, Janardhan HP, Trivedi CM, Pasparakis M,
1392 Kelliher MA (2018) RIP kinase 1-dependent endothelial necroptosis underlies systemic
1393 inflammatory response syndrome. *J Clin Invest* 128: 2064-2075

1394 Zhang T, Yin C, Boyd DF, Quarato G, Ingram JP, Shubina M, Ragan KB, Ishizuka T, Crawford JC,
1395 Tummers B *et al* (2020) Influenza Virus Z-RNAs Induce ZBP1-Mediated Necroptosis. *Cell* 180: 1115-
1396 1129 e1113

1397 Zhao J, Jitkaew S, Cai Z, Choksi S, Li Q, Luo J, Liu ZG (2012) Mixed lineage kinase domain-like is a
1398 key receptor interacting protein 3 downstream component of TNF-induced necrosis. *Proc Natl*
1399 *Acad Sci U S A* 109: 5322-5327

1400 Zhu X, Yang N, Yang Y, Yuan F, Yu D, Zhang Y, Shu Z, Nan N, Hu H, Liu X *et al* (2022) Spontaneous
1401 necroptosis and autoinflammation are blocked by an inhibitory phosphorylation on MLKL during
1402 neonatal development. *Cell Res* 32: 407-410

1403

1404

1405

Acknowledgements:

We thank James Vince, Jiyi Pang, David Tarlington, Angus Stock, Najoua Lalaoui, Asha Jois, Marcel Doerflinger, Quentin Gouil, Eric Hanssen and Bruce Rosengarten for constructive feedback and/or reagents during the preparation of this manuscript. We thank WEHI Monoclonal antibody facility for producing several antibodies used in this study. We thank the WEHI Histology team for high level support with immunohistochemistry. We thank the WEHI Bioservices team for high level support for animal experimentation, welfare, and ethics. We thank Kim Newton and Vishva Dixit for sharing the *Ripk3*$^{-/-}$ mice that were used to make the *Casp8*$^{-/-}$*Ripk3*$^{-/-}$ mice, and thank Michelle Kelliher for the *Ripk1*$^{-/-}$ mice that were used to generate the *Casp8*$^{-/-}$*Ripk1*$^{-/-}$*Ripk3*$^{-/-}$ mice. We thank Anaxis Pharma Pty Ltd for providing human RIPK3 expressing mice for our control experiments, and thank Andrew Kueh and Ueli Nachbur for their roles in generating this strain. We are grateful to the Department of Gastroenterology at the Royal Melbourne Hospital for performing endoscopies and to the patients who consented to donating their material to be used in this study.

Funding:

This work was supported by National Health and Medical Research Council of Australia (grants 1172929 to JMM, 2008652 to EDH, 2002965 to ALS, and the Independent Research Institutes Infrastructure Support Scheme 9000719), by the Kenneth Rainin Foundation (award to JMM, BC, AHA, ALS), and by the Victorian State Government Operational Infrastructure Support scheme. SC is supported by the WEHI Handman PhD scholarship, and AHA by the Avant Foundation, Crohn's and Colitis Australia and the University of Melbourne Scholarships. JMM and JS received research funding from Anaxis Pharma Pty Ltd, from which the salaries of KMP, AH, AL and PG were paid.

Conflict of interests:

KMP, SNY, AH, AL, PG, CRH, JD, IPW, JMH, JS, JMM and ALS have contributed to the development of necroptosis pathway inhibitors in collaboration with Anaxis Pharma Pty Ltd. YP is a co-holder of patent for material arising from this study. All other authors have no additional financial interests.

Abbreviations:

C8 (Caspase-8), C10 (Caspase-10), cl. C3 (cleaved Caspase-3), TNF (Tumour Necrosis Factor), RIPK1 (Receptor-interacting serine/threonine-protein kinase-1), pRIPK1 (phosphorylated RIPK1), RIPK3 (Receptor-interacting serine/threonine-protein kinase-3), pRIPK3 (phosphorylated RIPK3), MLKL (Mixed lineage kinase domain-like protein), pMLKL (phosphorylated MLKL), R1 (Receptor-interacting serine/threonine-protein kinase-1), R3 (Receptor-interacting serine/threonine-protein kinase-1), ML (Mixed lineage kinase domain-like protein), Nec1s (Necrostatin1s), WEHI (Walter and Eliza Hall Institute of Medical Research), WT (wild-type), KO (knockout), EV (Expanded View), IBD (inflammatory bowel disease), UC (ulcerative colitis), CD (Crohn's disease), SMA (smooth muscle actin), Kpf (Kupffer cell), endo (endothelial cell), p.o. (oral administration), i.p. (intraperitoneal administration), CV (central vein), PV (portal vein), BD (bile duct), CA (splenic central artery), WP (splenic white pulp), MZ (splenic marginal zone), RP (splenic red pulp), CRP (C-reactive protein), TS (Tumour Necrosis Factor and Smac mimetic), TSI (Tumour Necrosis Factor and Smac mimetic and IDN-6556), Ab (antibody), Uniform Manifold Approximation and Projection (UMAP), NP-KLH (4-hydroxy-3-nitrophenylacetyl hapten conjugated to keyhole limpet hemocyanin), CDS (coding sequence).

Figure legends:

Fig. 1. Automated immunohistochemistry shows constitutive necroptotic pathway expression is restricted. A To gauge immunohistochemistry performance, immunosignals from wild-type (WT) versus knockout (KO) tissue were deconvoluted, (i) pixel intensities plotted, (ii) ratioed to yield a signal-to-noise (S/N) histogram, and then (iv) integrated. **B** Heatmap shows relative integrated S/N values from 7 automated immunohistochemistry protocols across 7 tissues. Column headers indicate the antibody target clone name. Data are representative of n≥3 for each target and tissue. **C** Heatmap depicts relative protein abundance values as measured by (Geiger *et al.*, 2013). **D** Immunosignals of Caspase-8, RIPK1, RIPK3 and MLKL in wild-type versus the appropriate knockout (KO) tissue from *Mlkl*$^{-/-}$ or *Casp8*$^{-/-}$*Ripk3*$^{-/-}$ or *Casp8*$^{-/-}$*Ripk1*$^{-/-}$*Ripk3*$^{-/-}$. Data are representative of n≥3 for each target and tissue. Scale bars are 500µm. Related to Fig. **EV1**.

Fig. 2. Necroptotic potential is spatially graded across tissue zones. A Immunosignals of Caspase-8, RIPK1 and RIPK3 from wild-type mouse ileum (i), colon (ii), liver (iii) and spleen (iv). The crypt base (crypt), villi/crypt tip (tip), central vein (CV), portal vein (PV), bile duct (BD), central artery (CA), white pulp (WP), marginal zone (MZ) and red pulp (RP) are annotated. Inset of immunostaining in the ileum shows lower RIPK3 expression in Paneth cells (open arrowhead) relative to neighbouring cells. Arrow shows peri-central hepatocytes that express higher levels of Caspase-8. Closed arrowheads show Caspase-8^{+} RIPK1^{+} RIPK3^{+} Kupffer cells. Scale bars are 50µm, except for 10µm scale bar in inset. Data are representative of n≥3 for each target and tissue. **B** Relative expression levels of Caspase-8, RIPK1, RIPK3 (and splenic MLKL; Fig. **EV2B**) along the indicated tissue axes. Red datapoints indicate immunosignal intensities, and the overlaid dark blue line indicating the LOWESS best-fit along N=20 axes per tissue. Best-fit curves

are superimposed in the left-most column. Dashed line indicates the boundary between splenic white pulp and marginal zone. Data are representative of n>3 mice per target per tissue. **C** Scatterplots where each dot represents a different cell ontology from the *Tabula Muris* dataset *(Tabula Muris et al., 2018)*. The percent of cells within each ontology that expressed *Mki67*, *Ripk1* or *Ripk3* was plotted against that of *Top2a*. Pearson correlation coefficient values are shown. Related to Fig. **EV2**.

Fig. 3. RIPK3 expression is rapidly altered during systemic inflammation. A Experimental design. **B** Core temperatures of vehicle- and TNF-injected mice (n=3 mice per group). **C** Immunosignals for cleaved Caspase-3 (cl. C3), Caspase-8, RIPK1 or RIPK3 from the spleen of vehicle- or TNF-injected mice. Insets show unidentified RIPK1^{high} cells that associate with apoptotic bodies in splenic white pulp. **D** Graph of white pulp area occupied by cleaved Caspase-3^{+} material in vehicle- and TNF-treated mice. Each red datapoint represents one white pulp lobule (N=20 lobules/mouse). Blue datapoints indicate the median value per mouse (n=3 mice/treatment). Black bars represent the mean value per group. *p<0.05 by unpaired 2-tailed t-test. **E** RIPK3 immunosignals in colon of vehicle- or TNF-treated mice. **F** Best-fit curves of RIPK3 immunosignals along the crypt-to-tip axis from N=10 axes per mouse (n=3 mice/group). ***p<0.001 by multiple unpaired 2-tailed t-test. **G** RIPK3 (pink) and smooth muscle actin (brown) immunosignals in intestinal submucosa of vehicle- or TNF-treated mice. Insets show vessel cross-sections. Arrowheads show RIPK3^{+} endothelial cells (endo). **H** Plot of RIPK3 signals per vessel. Each red datapoint represents one vessel (N=50 vessels/mouse). Blue datapoints indicate the median value per mouse (n=3 mice/treatment). Black bars represent the mean value per group. *p<0.05 by unpaired 2-tailed t-test. **I** RIPK3 immunosignals in liver of vehicle- or TNF-treated mice. Central vein (CV), portal vein (PV) and Kupffer cell (Kpf). **J** Plot of RIPK3 signals per hepatocyte or Kupffer cell. Each transparent datapoint represents one

cell (N=90 cells/mouse). Opaque datapoints indicate the median value per mouse (n=3 mice/treatment). Black bars represent the mean value per group. *p<0.05 and **p<0.01 by unpaired 2-tailed t-test. **K** Core temperatures of vehicle-, TNF- and Nec1s+TNF-injected wild-type mice (n=4-5 mice/treatment; one dot/mouse/time). Line indicates mean. X indicates a euthanised mouse due to its body temperature being <30°C. **L** RIPK3 levels in serum from the mice in panel K or from untreated *Ripk3*$^{-/-}$ mice. Data expressed as arbitrary optical density units (A.U.). One dot per mouse. Mean ± SEM is shown. *p<0.05, **p<0.01 by 1-way ANOVA with Tukey's post-hoc correction.

Fig. 4. RIPK3 expression changes in response to dysbiosis. A Experimental design. **B** Bulk RNA sequencing was performed on indicated tissues. Heatmap depicts the log fold-change in gene expression for antibiotic- versus water-treated mice. Each row represents a different mouse. Legend shows the colour-to-value scale. **C** Immunoblots for the indicated proteins in the ileum and spleen of water- versus antibiotic-treated mice. Arrowheads indicate full-length proteins of interest. Coomassie staining of total protein content was used as a loading control. Data are representative of n=7 mice per tissue per group. **D** Caspase-8, RIPK3 and RIPK3 immunosignals in the ileum of water- or antibiotic-treated mice. Arrowheads to cytosolic accumulations of RIPK1 and RIPK3 in epithelial cells at villi tips. Scale bars in lower magnification micrographs are 100µm. Scale bars in insets are 10µm. Data are representative of n=7 mice per group. Related to Fig. **EV3**.

Fig. 5. Automated immunohistochemistry quantifies necroptotic signaling in human cells. A Immunosignals of cleaved Caspase-3, Caspase-8, RIPK1, RIPK3 and MLKL in wild-type versus *MLKL*$^{-/-}$ or *RIPK1*$^{-/-}$ or *CASP8*$^{-/-}$*CASP10*$^{-/-}$*MLKL*$^{-/-}$ HT29 cells. Arrowheads indicate Caspase-8^{+}, RIPK1^{+}, RIPK3^{+} and MLKL^{+} puncta that are presumed to be necrosomes. Data are representative of n≥2 for each protein and treatment. Scale bars in

lower magnification micrographs are 10µm. Scale bars in insets are 2µm. **B** The percent of cells per treatment group that contain cytosolic necrosome-like puncta immunostained by the stipulated antibody. N=1051-5630 cells were analysed per condition per stain. Data representative of n=2 experiments. **C** The number of puncta per cell. N=1000 cells per treatment group were analysed. Each datapoint represents one cell. Black bar indicates mean value. ****p<0.0001 by one-way ANOVA with Krukal-Wallis post-hoc correction. Data representative of n=2 experiments. Related to Fig. **EV5**, **EV6** and **EV7**.

Fig. 6. Case study for the detection of necroptotic signaling in inflammatory bowel disease. **A** Study design. **B** Blinded histopathological (Robarts Histopathology Index; RHI) scores of disease activity in intestinal biopsies relative to their endoscopic grading of inflammation. Diamond indicates a sample that could not be formally scored, as it was solely comprised of neutrophilic exudate, but was given a pseudo-score of 15 that likely underrepresents the extent of disease activity in this biopsy. Biopsies scored in Panel B were matched to those used in Panels C-E and Fig. **EV8** (see Table **1** for details). **C** Immunoblot of lysates from HT29 cells (red annotations) and intestinal biopsies from patients A-H (blue annotations). The fifth lane of each gel contained lysates from TSI-treated *RIPK3*$^{-/-}$ or TSI-treated *MLKL*$^{-/-}$ cells (see source data for details). Patients A,C,E,G were non-IBD controls. Patients B and D had ulcerative colitis (UC). Patients F and H had Crohn's disease (CD). The endoscopic grading of the biopsy site as 'non-inflamed', 'marginally inflamed' or 'inflamed' is stipulated. Closed arrowheads indicate full-length form of proteins. Asterisks indicate active, phosphorylated forms of RIPK3 (pRIPK3) and MLKL (pMLKL). Open arrowheads indicate active, cleaved forms of Caspase-8, Caspase-10 and Caspase-3. GAPDH was used as a loading control. **D** Immunohistochemistry for Caspase-8 (clone B.925.8) on intestinal biopsies. Insets a-e show diffuse epithelial Caspase-8 in patient C. Insets f-j show mild clustering of epithelial Caspase-8 and insets k-o show more

pronounced clustering of epithelial Caspase-8 in patient D (arrowheads). Scale bars in lower magnification micrographs are 500µm. Scale bars in insets are 10µm. **E** The number of Caspase-8^{+} puncta per 100 cells. Each datapoint represents one crypt. Whole slide scans with N=20246 cells from the 'non-IBD patient C' biopsy, N=10416 cells from the 'non-inflamed patient D' biopsy, and N=30799 cells from the 'inflamed patient D' biopsy were analysed. Black bar indicates mean value. **p<0.01 by one-way ANOVA with Tukey's post-hoc correction. Related to Table **1** and Fig. **EV8-10**.

EV Figures and Tables:

Fig. EV1. Optimisation pipeline for the immunohistochemical detection of the mouse necroptotic pathway. Summary of the steps used to test the specificity and to optimise the immunohistochemistry performance of monoclonal antibodies against mouse MLKL, RIPK3, RIPK1 and Caspase-8. Step 1: Immunoblot signals for each antibody on spleen homogenates from wild-type mice (WT) and *Mlkl*$^{-/-}$ or *Casp8*$^{-/-}$*Ripk3*$^{-/-}$ or *Casp8*$^{-/-}$*Ripk1*$^{-/-}$ *Ripk3*$^{-/-}$ mice (KO). Arrowheads indicate the full-length protein of interest. Representative GAPDH immunoblots are shown as loading controls. Data are representative of n=1-2 immunoblots per antibody. Steps 2-4: Heatmaps depict the integrated signal-to-noise values derived from immunohistochemical signals for each antibody on WT versus KO spleen sections. Legend shows the heatmap color-to-value scale. Step 2 varied the primary antibody concentration and the antigen retrieval pH. Step 3 varied the blocking reagent and the antigen retrieval time. Step 4 varied the amplification technique, amplification time, peroxidase treatment time and whether peroxidase treatment preceded/superceded primary antibody incubation. For each antibody, the optimal condition at Step 2 (white stars) was the starting point for Step 3. Similarly, the optimal condition for Step 3 was the starting point for Step 4. Yellow stars indicate the final

automated immunohistochemistry protocol stipulated in File **EV1**. Data in Steps 2-4 are representative of n=1-5 experiments per antibody per condition.

Fig. EV2. Constitutive co-expression of necroptotic effectors is confined to fast-cycling cells within progenitors, immune and barrier populations. A Heatmap of cell ontologies from the *Tabula Muris* dataset (Tabula Muris *et al.*, 2018). Left-most column depicts the tissue origin of each cell ontology. Other columns indicate the percent of cells within each ontology that expressed *Top2a, Mki67*, *Casp8*, *Ripk1, Ripk3* or *Mlkl*. Legend shows the color-to-tissue and the color-to-frequency scales. Cell ontologies of interest are annotated. **B** Micrograph of MLKL immunosignals from the wild-type mouse spleen. The white pulp (WP), marginal zone (MZ) and red pulp (RP) are annotated. Scale bar is 50µm. Scatterplot shows relative expression levels of MLKL along the white pulp-to-red pulp axis. Red datapoints show immunosignal intensities and the overlaid dark blue line indicates the LOWESS best-fit along N=20 axes from n=1 mouse. Dashed line indicates the boundary between splenic white pulp and marginal zone. Data are representative of n>3 mice. **C-D** Spatial transcriptomic data from (Moor *et al.*, 2018)) and (Ben-Moshe *et al.*, 2019) showing the relative expression levels (arbitrary units; A.U.) of Caspase-8, RIPK1, RIPK3 or MLKL along the ileal crypt-to-villus axis (Panel C) or the hepatic central vein-to-portal vein axis (Panel D). **E-G** Spatial transcriptomic data on mouse spleen 12 days after *Plasmodium berghei*-infection. Panel E shows a Uniform Manifold Approximation and Projection (UMAP) of cell populations distinguished by unsupervised leiden clustering. Legend shows the color assigned to each population. Panel F shows the location of each cell cluster. Scale bar is 500µm. Panel G shows the normalised expression for each gene product. Expression values for *Casp8*, *Ripk1*, *Ripk3* and *Mlkl* were summated to provide an index of 'cluster pathway expression', which was averaged to provide an index of 'zone pathway expression'. Data are from n=1 mouse.

Fig. EV3. Antibiotic-induced clusters of epithelial RIPK1/3 are not necrosomes. Immunoblots for the indicated proteins in homogenates of the ileum and spleen of water- versus antibiotic-treated mice or in mouse dermal fibroblasts (MDF) undergoing TNF-induced necroptosis (TSI). Arrowheads indicate full-length proteins of interest. Coomassie staining of total protein content was used as a loading control. Data are representative of n=7 mice per tissue per group.

Fig. EV4. RIPK3 is uniquely upregulated in splenic germinal centres. A Experimental design. **B** Ki67, Caspase-8, RIPK1, RIPK3 and MLKL immunosignals from adjacent sections of the naïve or NP-KLH-immunised mouse spleen. Arrowheads show a $Ki67^{+}$ germinal centre that co-stains for RIPK3, but not other members of the pathway. Representative of n>3 mice per group. Scale bars in lower magnification micrographs are 500µm. Scale bars in insets are 100µm. Data representative of n>3 mice per group. **C-H** *Ripk3*$^{-/-}$ or *Ripk3*$^{+/+}$ mice were immunised with NP-KLH and circulating NP-specific IgG_1 (Panel C), circulating NP-specific IgM (Panel D), splenic mature B cells (Panel E and F), splenic NP-specific plasma cells (Panel G), circulating low affinity NP-specific IgG_1 antibody (Panel H), circulating high affinity NP-specific IgG_1 (Panel H) and the ratio between circulating low-and-high affinity NP-specific antibody (Panel J) were measured at the indicated day after immunisation. Each datapoint represents one mouse. ns = non-significant by 2-sided t-test with Welch's correction.

Fig. EV5. Standardised quality control and optimisation of the immunohistochemical detection of human necroptotic proteins. Summary of the optimisation for immunodetection with monoclonal antibodies against human MLKL, RIPK3, RIPK1, Caspase-8 and Caspase-10 (C10). Step 1: Immunoblot signals for each antibody on

lysates from wild-type (WT) versus *MLKL*$^{-/-}$ or *RIPK1*$^{-/-}$ or *CASP8*$^{-/-}$*CASP10*$^{-/-}$*MLKL*$^{-/-}$ (KO) HT29 cells after treatment with the indicated stimuli. Arrowheads indicate the full-length protein of interest. Representative GAPDH immunoblots are shown as loading controls. Data are representative of n=1-2 immunoblots per antibody. Steps 2-4: Heatmaps depict the integrated signal-to-noise values derived from immunohistochemical signals for each antibody on WT versus KO HT29 cells. Legend shows the heatmap colour-to-value scale. Step 2 varied the primary antibody concentration and the antigen retrieval pH. Step 3 varied the blocking reagent and the antigen retrieval time. Step 4 varied the amplification technique, amplification time, peroxidase treatment time and whether peroxidase treatment preceded/superceded primary antibody incubation. For each antibody, the optimal condition at Step 2 (white stars) was the starting point for Step 3. Similarly, the optimal condition for Step 3 was the starting point for Step 4. Yellow stars indicate the final automated immunohistochemistry protocol stipulated in File **EV1**. Data in Steps 2-4 are representative of n=1-5 experiments per antibody per condition. The annotation 'see Fig. **EV1**' indicates optimisations that were only done using mouse tissues because these antibodies recognise both human and mouse orthologs.

Fig. EV6. Automated immunohistochemistry to detect necroptotic signaling in mouse cells. Immunosignals of cleaved Caspase-3, Caspase-8, RIPK1, RIPK3 and MLKL in wild-type mouse dermal fibroblasts. Arrowheads indicate Caspase-8^{+} or RIPK1^{+} puncta that are presumed to be necrosomes. Data are representative of n=1 for each protein and treatment. Scale bars in lower magnification micrographs are 10μm. Scale bars in insets are 1μm.

Fig. EV7. Assessing the specificity of immunostaining using wild-type, knockout and human RIPK3 knock-in mice. A Approach used to insert the human RIPK3 coding

sequence (CDS) into the mouse *Ripk3* locus. **B** Immunoblot of spleen homogenates from *Ripk3*$^{+/+}$, *Ripk3*$^{-/-}$, human RIPK3 (*RIPK3*$^{KI/KI}$) or hemizygous human RIPK3 (*Ripk3*$^{+}$*RIPK3*^{KI}) mice. GAPDH immunoblots are shown as loading controls. Each lane represents a different mouse. **C** Immunosignals produced by the anti-human RIPK3 (clone 37A7F) or anti-mouse RIPK3 (clone 8G7) antibodies on spleen sections from *RIPK3*$^{KI/KI}$, *Ripk3*$^{+/+}$ or *Casp8*$^{-/-}$*Ripk1*$^{-/-}$*Ripk3*$^{-/-}$. Data are representative of n≥3 for each target and tissue. Scale bars are 500µm.

Fig. EV8. Another instance of elevated intestinal apoptosis in a patient with ulcerative colitis. Immunoblot of lysates from HT29 cells (red annotations) and intestinal biopsies from patients A-H (blue annotations). The fifth lane of each gel contained lysates from TSI-treated *RIPK3*$^{-/-}$ or TSI-treated *MLKL*$^{-/-}$ cells (see source data for details). Patient J was a non-IBD control. Patient I had ulcerative colitis (UC). The endoscopic grading of the biopsy site as 'non-inflamed', 'marginally inflamed' or 'inflamed' is stipulated. Closed arrowheads indicate full-length form of proteins. Asterisks indicate active, phosphorylated forms of RIPK3 (pRIPK3) and MLKL (pMLKL). Open arrowheads indicate active, cleaved forms of Caspase-10 and Caspase-3. GAPDH was used as a loading control.

Fig. EV9. Atlas of necroptotic pathway expression in human intestinal crypts. Immunohistochemistry for cleaved Caspase-3, Caspase-8 (clone B.925.8), RIPK1, RIPK3 and MLKL (clone EPR171514) on intestinal biopsies from the stipulated patients. Four representative micrographs per biopsy are shown (i-v). Open arrowheads indicate instances of epithelial apoptosis. Closed arrowheads indicate instances of epithelial Caspase-8 clustering. Scale bars are 10µm. The location for each micrograph within the biopsy is indicated in Fig. **EV10**.

Fig. EV10. Atlas of necroptotic pathway expression in a cohort of human intestinal biopsies. Immunohistochemistry for cleaved Caspase-3, Caspase-8 (clone B.925.8), RIPK1, RIPK3 and MLKL (clone EPR171514) on intestinal biopsies from the stipulated patients. The insets show the location of each micrographs in Fig. **EV9** (annotated as i-v per biopsy). Scale bars are 100µm.

Table 1. Patient and clinical data related to **Fig. 6**.

File EV1. The automated immunohistochemical staining protocols used in this study will be provided upon final publication.

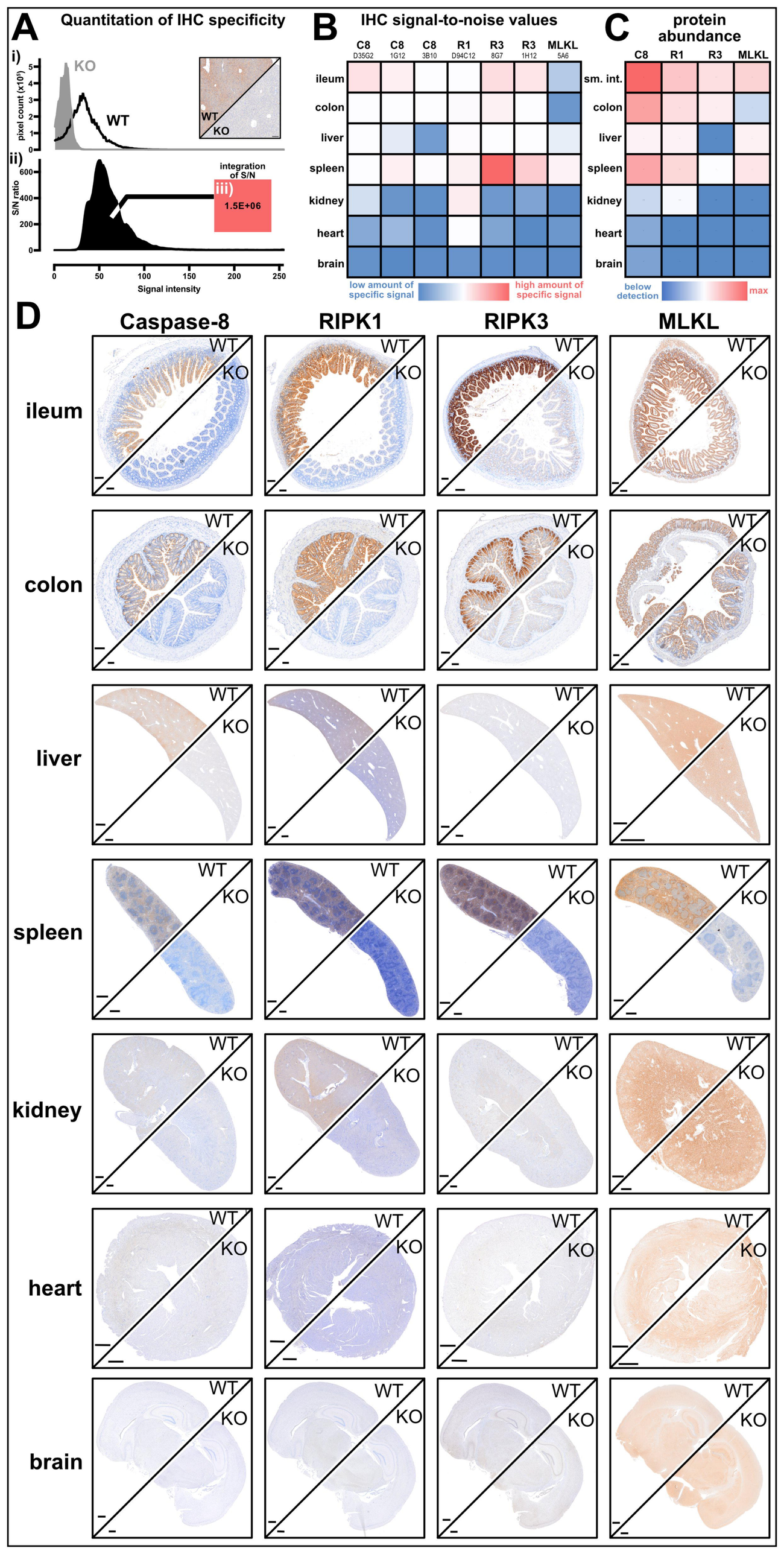
A
Quantitation of IHC specificity
i)
KO
WT
pixel count (x10⁶)
WT
KO
ii)
S/N ratio
integration of S/N
iii)
1.5E+06
Signal intensity
B
IHC signal-to-noise values
C8 D35G2
C8 1G12
C8 3B10
R1 D94C12
R3 8G7
R3 1H12
MLKL 5A6
ileum
colon
liver
spleen
kidney
heart
brain
low amount of specific signal
high amount of specific signal
C
protein abundance
C8
R1
R3
MLKL
sm. int.
colon
liver
spleen
kidney
heart
brain
below detection
max
D
Caspase-8
RIPK1
RIPK3
MLKL
ileum
colon
liver
spleen
kidney
heart
brain
WT
KO

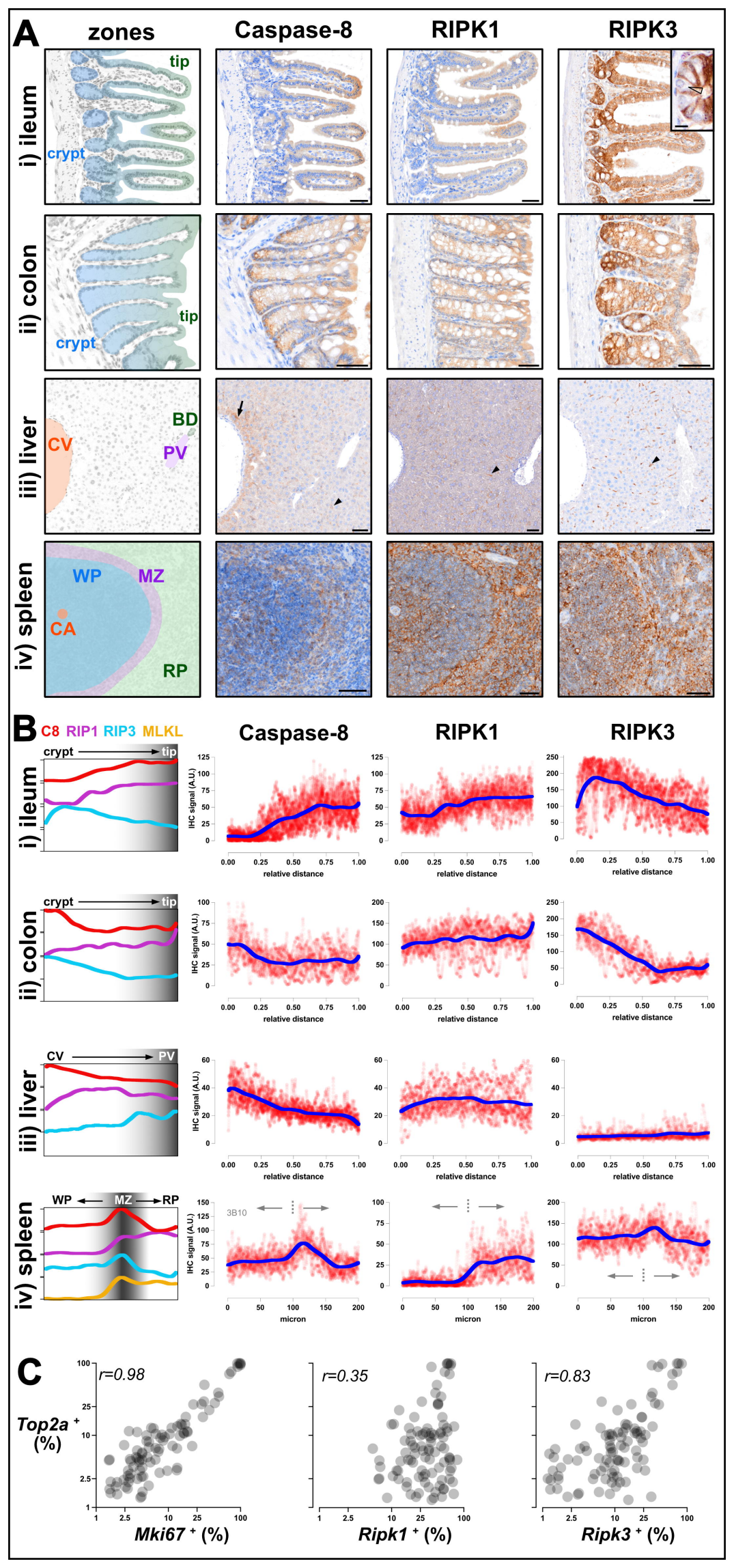
A
zones
Caspase-8
RIPK1
RIPK3
i) ileum
tip
crypt
ii) colon
tip
crypt
iii) liver
BD
CV
PV
iv) spleen
WP
MZ
CA
RP
B
C8 RIP1 RIP3 MLKL
Caspase-8
RIPK1
RIPK3
i) ileum
ii) colon
iii) liver
iv) spleen
crypt
tip
CV
PV
WP
MZ
RP
IHC signal (A.U.)
relative distance
micron
3B10
C
r=0.98
r=0.35
r=0.83
Top2a + (%)
Mki67 + (%)
Ripk1 + (%)
Ripk3 + (%)

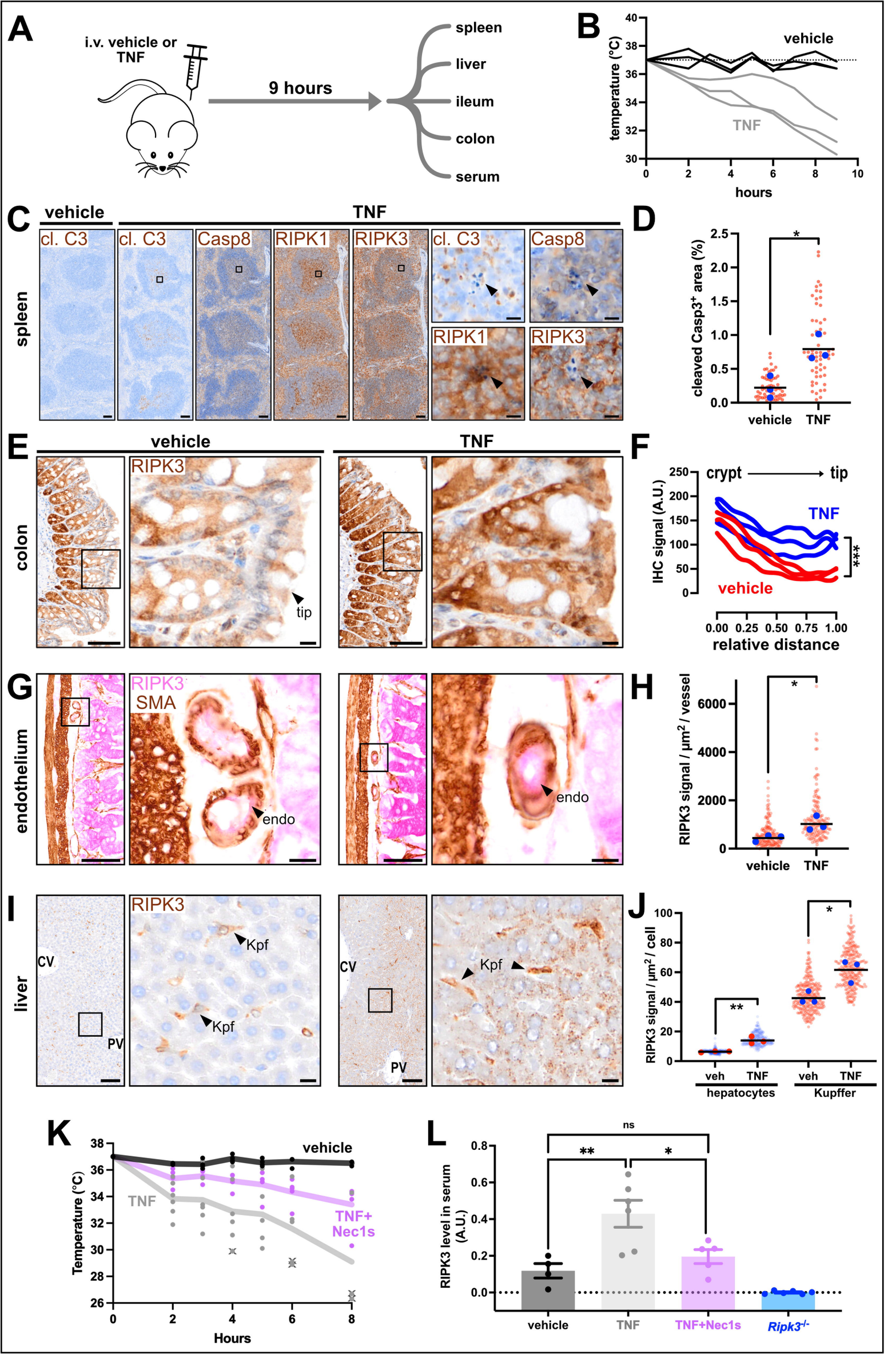
A
i.v. vehicle or TNF
9 hours
spleen
liver
ileum
colon
serum
B
temperature (°C)
vehicle
TNF
hours
C
vehicle
TNF
spleen
cl. C3
Casp8
RIPK1
RIPK3
D
cleaved Casp3+ area (%)
vehicle
TNF
E
colon
RIPK3
tip
F
crypt
tip
IHC signal (A.U.)
TNF
vehicle
relative distance
G
endothelium
SMA
endo
H
RIPK3 signal / µm² / vessel
I
liver
CV
PV
Kpf
J
RIPK3 signal / µm² / cell
veh
hepatocytes
Kupffer
K
Temperature (°C)
TNF+ Nec1s
Hours
L
RIPK3 level in serum (A.U.)
ns
TNF+Nec1s
Ripk3-/-

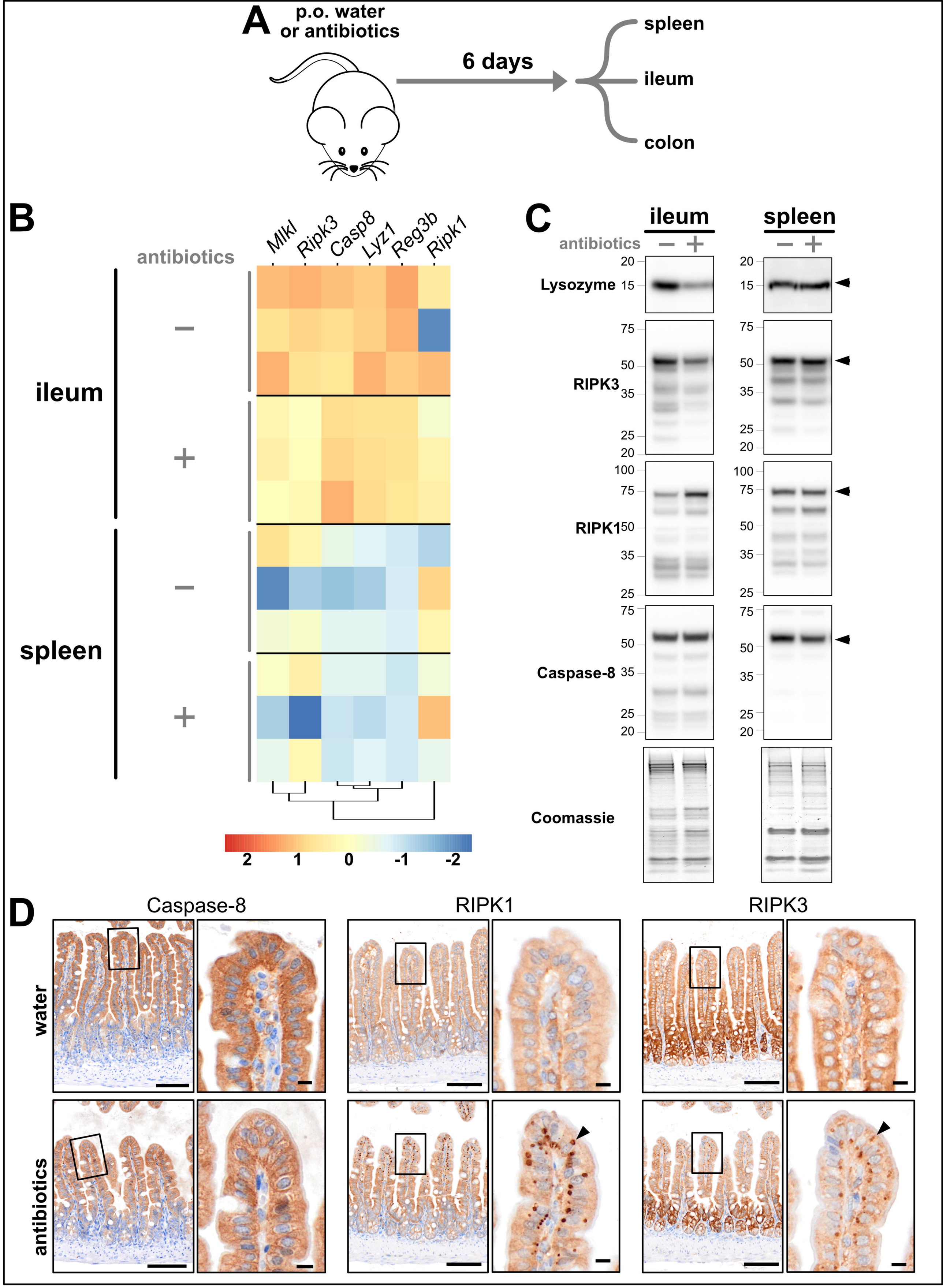
A
p.o. water
or antibiotics
6 days
spleen
ileum
colon
B
antibiotics
Mlkl
Ripk3
Casp8
Lyz1
Reg3b
Ripk1
ileum
spleen
−
+
−
+
2
1
0
-1
-2
C
ileum
spleen
antibiotics
− +
− +
Lysozyme
RIPK3
RIPK1
Caspase-8
Coomassie
20
15
75
50
35
25
20
100
75
50
35
25
75
50
35
25
20
D
Caspase-8
RIPK1
RIPK3
water
antibiotics

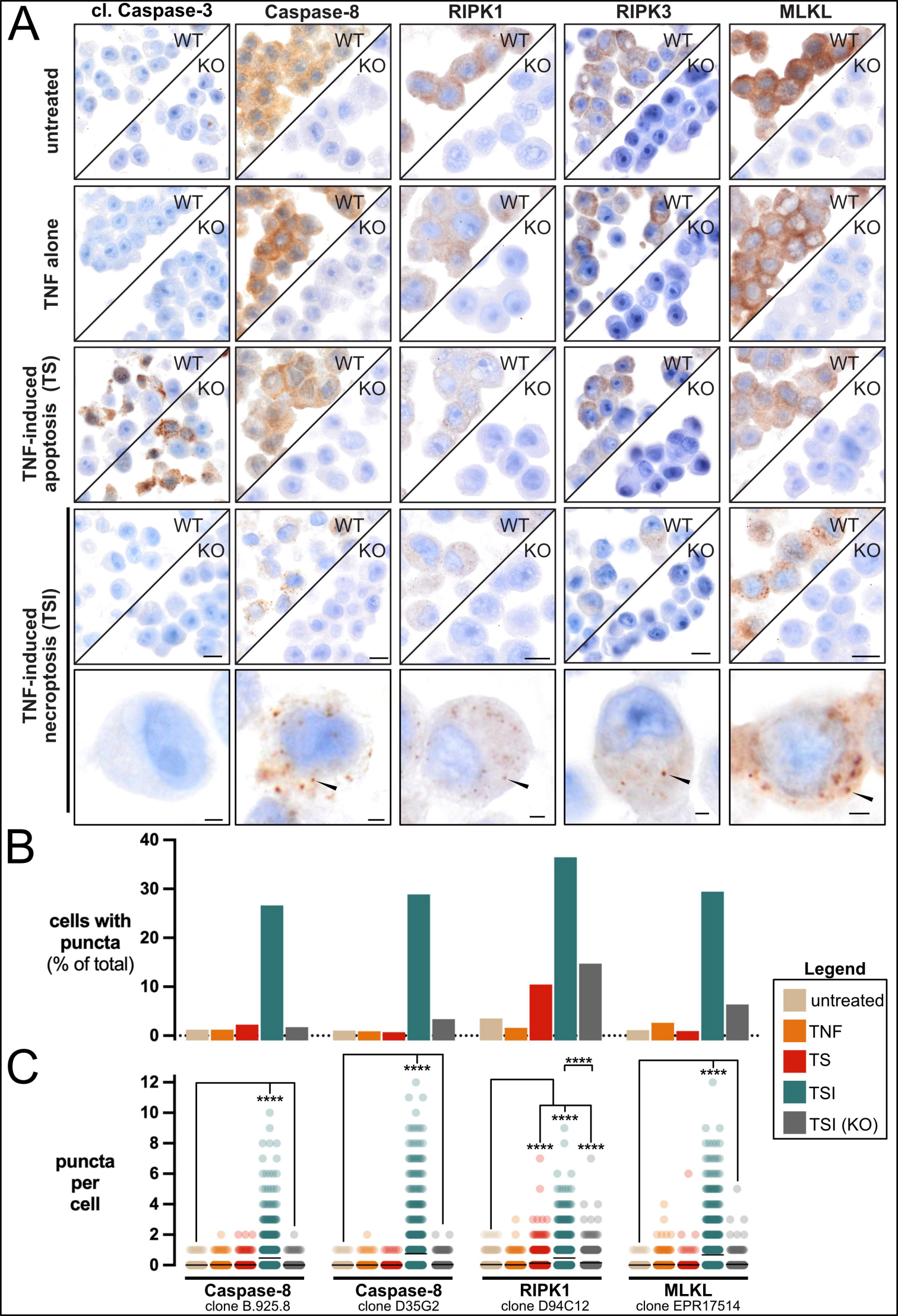
A
cl. Caspase-3
Caspase-8
RIPK1
RIPK3
MLKL
untreated
TNF alone
TNF-induced apoptosis (TS)
TNF-induced necroptosis (TSI)
WT
KO
B
cells with puncta (% of total)
40
30
20
10
0
Legend
untreated
TNF
TS
TSI
TSI (KO)
C
puncta per cell
12
10
8
6
4
2
0
****
Caspase-8 clone B.925.8
Caspase-8 clone D35G2
RIPK1 clone D94C12
MLKL clone EPR17514

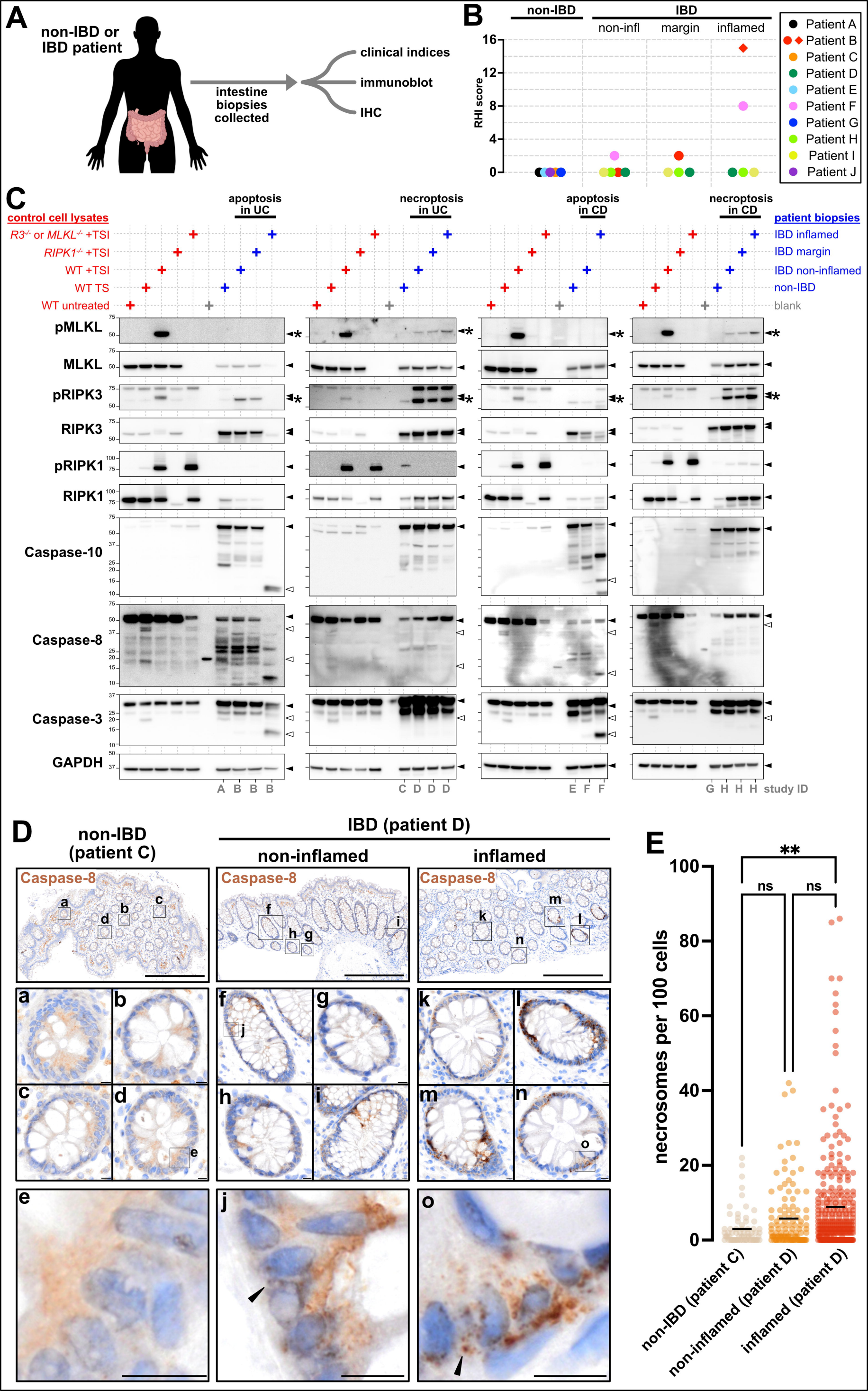
A
non-IBD or IBD patient
intestine biopsies collected
clinical indices
immunoblot
IHC
B
non-IBD
IBD
non-infl
margin
inflamed
RHI score
Patient A
Patient B
Patient C
Patient D
Patient E
Patient F
Patient G
Patient H
Patient I
Patient J
C
control cell lysates
apoptosis in UC
necroptosis in UC
apoptosis in CD
necroptosis in CD
patient biopsies
R3-/- or MLKL-/- +TSI
RIPK1-/- +TSI
WT +TSI
WT TS
WT untreated
IBD inflamed
IBD margin
IBD non-inflamed
non-IBD
blank
pMLKL
MLKL
pRIPK3
RIPK3
pRIPK1
RIPK1
Caspase-10
Caspase-8
Caspase-3
GAPDH
A B B B
C D D D
E F F
G H H H
study ID
D
non-IBD (patient C)
IBD (patient D)
non-inflamed
inflamed
Caspase-8
E
necrosomes per 100 cells
ns
ns
**
non-IBD (patient C)
non-inflamed (patient D)
inflamed (patient D)